# Acoustic Concepts in Micro-Scale Flow Control and Advances in Modular Microfluidic Construction

by

Sean Michael Langelier

A dissertation submitted in partial fulfillment
of the requirements for the degree of
Doctor of Philosophy
(Chemical Engineering)
in The University of Michigan
2010

Doctoral Committee:

Professor Mark A. Burns, Chair
Professor Karl Grosh
Professor Erdogan Gulari
Professor Robert M. Ziff


*Melancholia* by Albrecht Dürer

for my parents

# ACKNOWLEDGEMENTS

There is simply too much to say here, but I would be remiss if I didn't at least try. I must first acknowledge my parents, Kathleen Mary McQuilkin and Kenneth Paul Langelier, whose unending love and support and sacrifice figures so heavily in the completion of this dissertation. I must also acknowledge Dan Brown. My passion for music, which gives me so much joy and escape, is in large part his doing. I wish to express my deepest gratitude to all of my wonderful friends and family — you know who you are — whose kindness, patience, and character continue to provide meaning and perspective in my life. Lastly, I want to give special thanks my dissertation advisor Prof. Mark A. Burns whose imprimatur of scholarship, class, and guidance have been my privilege to receive these five years.

# TABLE OF CONTENTS

# LIST OF FIGURES

**Figure**

# ABSTRACT

Acoustic Concepts in Micro-scale Flow Control and Advances in Modular Microfluidic Construction

by

Sean Michael Langelier

Chair: Mark A. Burns

Despite thirty years of research, the full scientific and social impact of microfluidics has not been realized. This dissertation focuses on addressing two key issues to accelerate this realization: micro-scale flow control and microfluidic device construction. We introduce the design of a new acoustic-based mechanism for multiplexed pressure-driven flow control. The device we have developed converts the frequency content of an acoustic signal into four individually addressable pressure outputs, tunable over a range 0-200 Pa with a control resolution of 10 Pa. The pressure generating components of the device consist of a bank of four resonance cavities (404, 484, 532, and 654 Hz), each with an attached rectification structure. We demonstrate how this scheme can be used for programmatic operation of both droplet-based and continuous-flow microfluidic systems using only a single control line. We then explore an alternative acoustic actuation scheme involving frequency dependent attenuation within finite phononic crystals. Specifically, finite element analysis of the band properties of periodic two-dimensional microstructures subject to a variety of geometric lattice perturbations is presented. Phononic structures with periodicity over the range of 100-1400

$\mu$m were found to exhibit rich band gap effects over 100-300 kHz. We also discuss the utility of one-dimensional transfer matrix method approximations and analysis in the infinite limit as methods for understanding and predicting crystal transmission. Lastly, we describe an advanced modular microfluidic construction scheme using pre-fabricated polymeric building blocks (MABs) that can be assembled into working devices on-site within minutes. We discuss: (1) development of flexible silicone casting trays for dramatically improved production and extraction of MABs, (2) reliable "off-the-shelf" preparation of 1-3 $\mu$m PDMS thin films for facile block assembly with simultaneous block/block and block/substrate bonding, and (3) modification of MAB block design to include self-alignment and sealing structures. Completed MAB assemblies possessed an average channel offset of $\pm 12\mu$m, an average channel angle of $\pm 1$ degree, and were found to exhibit the fewest inter-block gaps at a piece convexity of 0 $\mu$m. Exemplary MAB devices for performing on-chip gradient synthesis, droplet generation, and total internal reflectance microscopy are also presented.

# CHAPTER I

# INTRODUCTION

## 1.1 Motivation

Microfluidics emerged in the late 1980s from advances in liquid chromatography. Later, IBM — in the first major technological adaptation of micro-scale fluid physics — developed the ink-jet print head which quickly usurped the (then dominant), dot-matrix technology. In the years that followed, the desire for precise control of minute ($\mu$L and pL) liquid volumes spawned innumerable applications and commercial ventures, each seeking to leverage the many now broadly accepted, advantages of working in a micro-environment (*e.g.*, reduced reagent consumption and cost, shorter analysis times, parallelization, and portability). But, even with this attention as well as a surge in publications in the early 2000s, microfluidics remains a niche technology falling well short of early predictions for the field.

One issue preventing the widespread adoption of microfluidic technologies relates to the difficulties associated with micro-scale flow control. Here, the challenge is to orchestrate the coordinated manipulation of small liquid volumes to and from various unit operations on a microfluidic chip in order to perform a given experiment. Such a task requires very precise control of the fluidic driving force — mechanistically, this is typically accomplished using either pressure-driven or electrokinetic means — and is often problematic because many of the actuation mechanisms available are not suited

to output the small pressure differences needed for microfluidic control. A second issue, perhaps only relevant to academia, is that a technology gap typically exists between the developers of microfluidic tools and end users, the majority of which reside in the life sciences. Here, researchers who might otherwise benefit from the application of microfluidic tools in areas such as high-throughput drug screening or cell culture, are deterred by the high cost and expertise required to design and fabricate custom microfluidic systems. Thus, the task(s) facing developers of microfluidic technologies — if the full impact of these tools is to be realized — is the creation of more advanced solutions for micro-scale flow control and development of novel fabrication strategies that facilitate use by non-experts.

## 1.2 Mechanisms of Micro-Scale Flow Control

Micro-scale flow control is typically accomplished using either an electrokinetic or pressure-driven approach, each of which has its own unique set of actuation mechanisms, and each with its own advantages and limitations. In the electrokinetic approach, an electric field is applied as a means of generating force on fluids and particles [1]. Perhaps the most traditional embodiment of this mechanism is electroosmotic flow (EOF). In EOF, a diffuse charge layer at the interface of a liquid electrolyte and a dielectric migrates toward the electrode of opposite polarity and, in the process, drags the bulk fluid along with it. The implementation of EOF is simple, requiring only an appropriate voltage source, and to its credit, EOF has been shown to be effective for simultaneous control of multiple fluidic inputs [2]. However, EOF cannot be used to control gases, non-polar liquids, or discontinuous liquid phases, and it is extremely sensitive to dielectric surface properties, impurities, and channel layout. Electrothermal flow is also possible and arises from temperature gradients stemming from joule heating in the working fluid [3]. This approach is rarely used, however, as it often leads to electrochemical dissociation of the working fluid and

electrode corrosion.

So-called digital microfluidic systems make use of various actuation mechanisms such as electrowetting on dielectric (EWOD) to manipulate droplets on the surface of planar substrates which have been coated with a dielectric [4]. EWOD is advantageous as it eliminates the leakage and bonding issues associated with fabricating enclosed micro channels and is highly amenable to automation. However, EWOD suffers from evaporation issues and is, as are all electrokinetic mechanisms, limited to the manipulation of aqueous electrolytes.

Pressure-driven flow schemes, both passive and active, work by generating pressure differentials within the working fluid. Passive actuation mechanisms such as capillary pressure are unique in that they do not require external energy input in order to function. Instead, flow in a passive system occurs spontaneously as a product of an engineered interplay between capillary forces, surface tension, and channel geometry [5]. Such systems, though ideal for simple unidirectional fluid transport, lack the operational versatility necessary for complex flow control due to their deterministic flow paths and designed dependence on specific liquid/surface properties.

Active pressure-driven mechanisms, by contrast, are extremely versatile, generally indifferent to fluid properties and channel geometry, and have the additional benefit of being dynamically reconfigurable. The simplest active pressure generating components, *e.g.* syringe pumps and pneumatics, work by direct application of external pressure and are ideal for continuous flow applications such as particle synthesis [6], where large stable flows are required. Reciprocating displacement mechanisms are typically microfabricated and work by coupling the oscillatory deflection of a diaphragm with some form of fluidic rectification structure [7, 8]. However, these systems are extremely difficult to fabricate and are prone to mechanical fatigue/failure. Other, non-mechanical, approaches such as centrifugal force [9], and acoustic streaming [10] have also been demonstrated.

## 1.3 Trends in Microfluidic Device Construction

Traditional microfabrication is performed in a clean-room environment using specialty photolithographic equipment. Unfortunately, these facilities and instruments are extremely expensive and often require significant operational expertise, thus alienating a large population of users (primarily in the life sciences) who might otherwise benefit from the technology. In recent years, there have been numerous attempts to lower this entry barrier by introducing fabrication pathways that minimize dependence on costly clean-room lithography.

Duffy et al. introduced the use of high-resolution transparencies and elastomeric casting or soft lithography, in favor of costly chrome photomasks and hazardous wet chemical etch steps [11]. Others aimed to eliminate photomasks entirely using a direct print approach — with laser toner serving as the mold structures [12, 13]. Limitations of achievable feature depths using the direct print approach then led to the use of solid object printing [14]. More recently, the trend has shifted to modular microfluidic construction. These strategies do away with the entire microfabrication process, and instead deliver to the end user, sets of pre-fabricated components which can be assembled at the point of use [15–18].

## 1.4 Organization of this Dissertation

This dissertation explores the use of acoustic mechanisms for advanced microscale flow control as well as the use of a modular assembly block platform for simple microfluidic device construction. In Chapter 2, we introduce a new acoustic-based method for multiplex pressure-driven flow control of microfluidic devices. We describe an acoustically-actuated flow control mechanism whereby the frequency content of an acoustic input signal is converted into a set of four independently addressable output pressures. The function of the prototype device which is comprised of a bank of

tuned resonance cavities with attached rectification structures is then discussed, and the characterization of the individual components presented. We demonstrate how this scheme can be used, in conjunction with computer control, to perform precise droplet positioning tasks as well as merging, splitting, and sorting within branched microfluidic networks. We further show how this scheme can be implemented for control of continuous-flow systems, specifically for generating acoustically-tunable liquid gradients. Last, we discuss the potential miniaturization of the concept for embedded multiplexed flow control.

The theoretical investigation of an alternative acoustic actuation strategy using phononic crystals is explored in Chapter 3. Here, we perform a detailed study of the geometric properties of micro-scale two-dimensional phononic crystals as they relate to the emergence and evolution of acoustic transmission band gaps. Using a simple cubic lattice comprised of rigid cylindrical inclusions as a point of departure, we compute transmission coefficients for crystals with a wide array of geometric properties using finite element simulations. We further explore the use of a one-dimensional transfer matrix method as a computationally leaner alternative for predicting acoustic transmission near the band gap. Calculated band structures, *i.e.* maps of crystal transmission in the infinite limit, are also discussed as an aid for analyzing the transmission data of finite systems.

In Chapter 4 we present an advanced modular microfluidic assembly block approach designed to facilitate microfluidic device construction among non-experts. We first describe the fabrication methodology by which pre-formed polymeric building blocks (MABs) possessing a variety of fluidic channel layouts, are linked together and bonded to form functional microfluidic devices. Next, we introduce a new process for the fabrication of the MABs themselves utilizing flexible silicone molds for improved casting and extraction. We go on to discuss the benefits of performing MAB assembly on pre-coated glass substrates and present instructions for their preparation.

We describe modifications to the MAB block design for minimizing discrepancies in alignment angle, offset, and inter-block gaps. We then report on several exemplary applications of MAB devices including: synthesis of controlled chemical gradients, rapid droplet generation, and total internal reflectance spectroscopy. We finish by discussing the future of the MAB approach, focusing specifically on optimization of mold lithography and the potential for three-dimensional MAB structures.

# CHAPTER II

# ACOUSTICALLY-DRIVEN PROGRAMMABLE LIQUID MOTION USING RESONANCE CAVITIES

## 2.1 Introduction

Microfluidic systems continue to rely on externally applied pressures for the manipulation of fluid samples. As such, operation of a chip can often require extensive off-chip control equipment. Syringe pumps (displacement pumps), for instance, though ideal for continuous flow applications such as organic/particle synthesis [6, 19–21], and droplet generation [22] are impractical for control of complex microfluidic d evices, as each fluid input requires a dedicated pump. Manipulation of discrete fluid droplets, on the other hand, is typically accomplished using air pressure [23]. However, careful attention needs to be paid to the magnitude of the pressure gradient [24] as most bench scale regulators are not designed to produce the minute pressure differences needed for precise droplet control.

Many researchers introduce pressure attenuation mechanisms to circumvent large and undesirable pressure gradients. For example, Pal *et al.*, employed intermittent pulsing of a coarsely regulated pressure source [25] to precisely position drops. Reciprocating displacement micropumps constitute a popular choice for on-chip pressure

generation [7]. These pumps operate by pairing the displacement of a diaphragm, typically driven piezoelectrically, with some form of rectification structure. But, despite the remarkable performance of these and other on-chip pressure sources, they possess many of the same limitations as their macroscopic counterparts. Chang *et al.* report on a novel approach to distributed pressure control using microfabricated Venturi nozzles whereby coarsely regulated air pressure is converted into pressures better suited for droplet control [26]. Hybrid schemes employing both displacement and direct pressure are also possible, most notably, for serial deflection of elastomeric membranes [27]. But despite multiplexing efforts aimed at reducing the number of external control variables [28], the number of off-chip connections and control equipment necessary to operate a reasonably complex device can remain prohibitively large.

Apart from conventional pressure-driven mechanisms, on-chip acoustic based methods for fluidic actuation are becoming increasingly common in areas ranging from fluid transport [29, 30], mixing [10], separations [31] and droplet sequestering [32]. Acoustic streaming, also known as quartz wind, is a phenomenon by which steady momentum flux is imparted to a fluid by the impingement of high amplitude acoustic waves. Bulk fluid motion can result from the build up of a non-linear viscous Reynolds stress at the incident fluid boundary [33]. Microfluidic applications utilizing acoustic streaming have thus far been limited primarily to driving closed loop fluid circuits [8, 34] mainly due to extremely low back pressure tolerance on the order of 1 Pa. Surface acoustic wave or SAW devices also utilize acoustic streaming but operate on open planar surfaces rather than within closed channels. SAWs can be launched in piezoelectric substrates by application of resonant frequencies to sets of interdigitated electrodes with the resonant frequencies determined by electrode spacing. SAWs, in conjunction with hydrophobically altered surfaces, are attractive for microfluidic control as droplets residing in the path of a launched wave undergo a rolling motion due to acoustic streaming at the leading pinned meniscus of the drop.

As such, the SAW platform can be used to position droplets arbitrarily along the lines of intersecting electrode paths.

We have devised a novel distributed pressure control scheme that employs acoustic resonance cavities and rectification structures to translate the frequencies contained in an acoustic signal into separately addressable output pressures that can be used to control liquids in a microfluidic device. Unlike any pressure control scheme we are aware of, the device is capable of simultaneously controlling multiple output pressure signals, in either a pulsed or continuous fashion, over a range of approximately 0-200 Pa with a control resolution of 10 Pa. These capabilities eliminate the need for pressure attenuation mechanisms, reduce external control infrastructure, and greatly improve upon the backpressure tolerance of acoustic streaming based methods.

## 2.2 Results and Discussion

Operation of a microfluidic device using musical tones to induce motion is accomplished with a form of pneumatic decoding similar to what occurs in fiber optic electronic communication. An encoded acoustic signal composed of a specific blend of resonant tones is decoded and transduced into a set of discrete pneumatic signals proportional to the tonal content. This transduction occurs in two parts: First, acoustic cavities experience a dramatic increase in sound pressure when exposed to a resonant tone. Second, rectification structures attached to the cavities convert the amplified oscillating pressures into net unidirectional flows. As an example of this transduction, a programmed sequence of musical tones (Figure 2.1c: *Tone Sequence*) was synthesized on a computer and delivered to a bank of four resonance cavities (Figure 2.1a) with principal resonance modes at 404 Hz, 484 Hz, 532 Hz and 654 Hz, respectively. The outlet flow rate from each cavity was monitored using a hot-wire anemometer and, while each cavity is subject to the same input, their output is frequency dependent (Figure 2.1c). Specifically, the input sequence, which grows

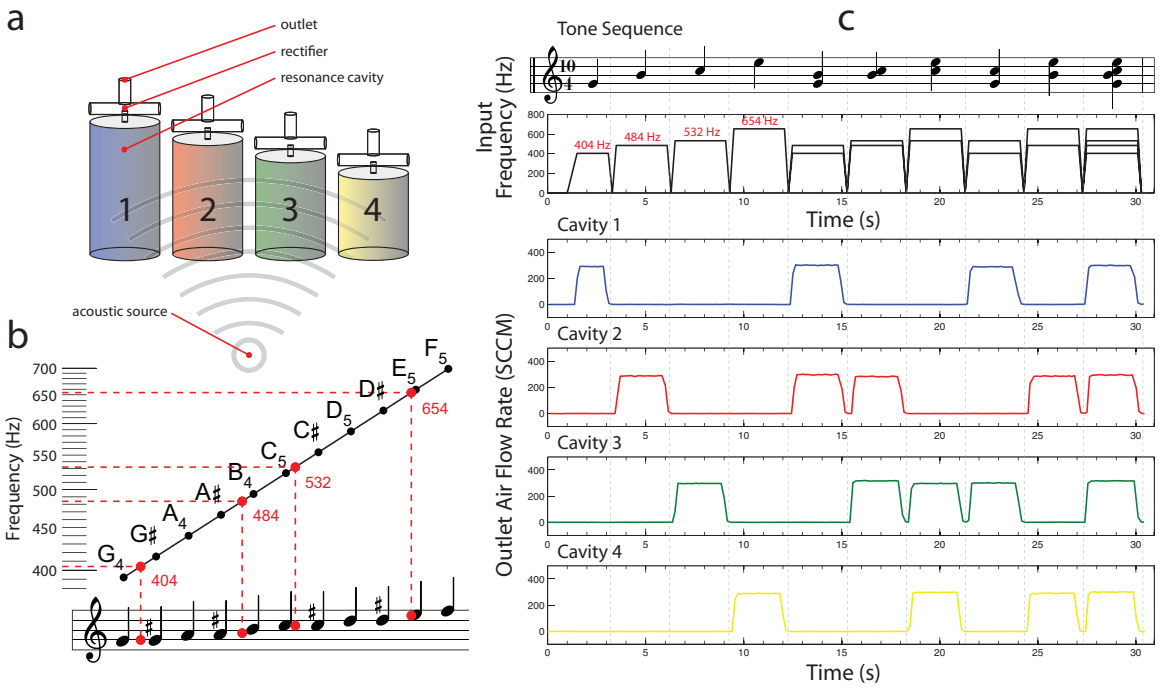


Figure 2.1: Resonance triggered air-flow study. (a) Conceptual representation of the device illustrating key components subject to the same acoustic input. (b) Location of cavity resonance frequencies on the chromatic scale. (c, *Tone Sequence*) Input acoustic signal represented both graphically and musically by proximity to nearest semitone on the chromatic scale. (c, bottom) Outlet flow rate as a function of time recorded at the outlets of the four rectification structures. Output for each resonance cavity is stable, responsive to a single musical queue, and insensitive to the presence of other competing tones.

in complexity during the experiment, triggers an output only at the cavities whose resonant tones were present. Figure 2.1 also shows that each cavity exhibits a stable and repeatable step-like response to its resonant tone and that the presence of other competing tones produces no spurious output. For the sake of graphical clarity, as well as a demonstration of flow control, the output flow rate of each cavity was set to approximately 300 standard cubic centimeters per minute (SCCM). However, using the computerized interface linked to the device, it is trivial to adjust the output flow characteristics of any specific cavity simply by adjusting the relative strength of the tone in the input waveform.

### 2.2.1 Acoustic Resonance

Perhaps the most intriguing facet of this control scheme is the use of resonance cavities as pneumatic decoders, a concept first explored by Rudolph Koenig (ca. 1880) who used an apparatus comprised of a bank of Helmholtz resonators as a means of dissecting the frequency content of sound. Decoding, in this context, refers to the selective and non-destructive amplification of target frequencies from a complex acoustic excitation. Each of the four acoustic cavities in our device, in effect, plucks from the ambient sound field the frequency at which it prefers to oscillate and amplifies that signal, producing a local oscillating cavity pressure significantly greater than that of the incident wave. Amplification in this case occurs due to standing wave resonance (SWR), a phenomenon that describes the addition of an incident wave and its reflections within an acoustic cavity (*i.e.* the geometry of the cavity is such that incident wave fronts combine perfectly with oppositely traveling reflections). In a so-called "quarter-wavelength" resonator, such as those employed here, the principle resonance occurs at a frequency whose quarter wavelength is equal to the axial cavity length. Higher harmonics, in the case of a quarter wavelength resonator can occur at odd integer multiples of the principle.

Resonance spectrographs (Figure 2.2a) were obtained by subjecting the device to a range of frequencies at constant voltage while monitoring outlet flow rate. The emergence of highly elevated peaks in outlet flow corresponds, as mentioned above, to the principal SWR mode of each cavity. Over the frequency domain sampled, each cavity is sympathetic to exactly one narrow, non-overlapping band of frequencies, the width and spacing of which determines, for a limited frequency range, the number of independent pressure outputs that may be controlled. For example, using an average peak width of 21±10 Hz from Figure 2.2 and a frequency range of 808±50 Hz computed as the difference of the first harmonic and the lowest principle (*i.e.* 1212 Hz - 404 Hz), the number of cavities and, therefore, signals that can theoretically be con-

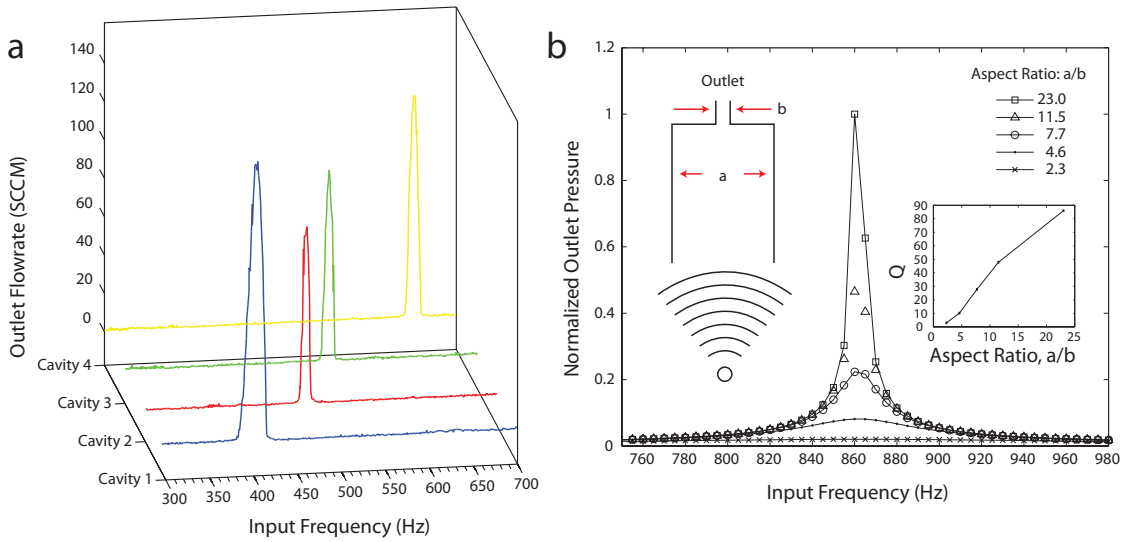


Figure 2.2: Acoustic resonance performance of the device. (a) acoustic resonance spectrograph representing the acoustic response of each cavity (1-4) subject to a steadily ramped input frequency at constant power. Cavities 1-4 exhibit marked SWR peaks at 404 Hz, 484 Hz, 532 Hz and 654 Hz, respectively. (b) Two-dimensional incompressible flow FEM simulation result for an arbitrary cavity exhibiting resonance at 860 Hz illustrating the effect of increased radiation losses on Q for the aspect ratios: 2.3, 4.6, 7.7, 11.5, and 23.

trolled is 38±18. However, with improved cavity design, the number of independent signals can be significantly higher than this number.

The sharpness of a resonance peak is related to the quality of resonance (Q = the ratio of stored-to-radiated acoustic energy per cycle). Quantitatively, we can define Q as the resonance frequency divided by the peak bandwidth at half of the maximum value. With respect to the device presented here, cavities with high Q values are preferred as they minimize the required input energy and allow for a greater number of cavities to be situated in a finite frequency domain. To understand the role of our cavity geometry as it pertains to Q, finite element simulations were performed for a simplified two-dimensional geometry varying the ratio of the cavity diameter to the outlet port diameter. In Figure 2.2b, we notice that Q decreases with decreasing aspect ratio, a result consistent with the intuitive suspicion that increases in the relative diameter of a radiation port cause a proportionate increase in radiation loss.

### 2.2.2 Rectification

Rectification structures are critical to the working concept of the device. In general, the role of such structures in the context of fluid flow is to introduce a directional bias in the flow thereby imparting a preferred flow direction from an oscillating input. The bias itself can be implemented using a moving structure as in the case of a check or flap valve, or alternatively, using stationary structures and exploiting a physical property of the working fluid. For an inertial rectifier [35] such as the one we have employed here (schematic inset, Figure 2.3) a synthetic jet [36] is used to introduce an asymmetry in the flow leaving the rectifier outlet. During operation, vibrating air within each cavity serves as an oscillating input pressure source to the rectifier. Only under resonant excitation is the pressure gradient of the oscillating flow field of sufficient strength to form a synthetic jet.

Figure 2.3 presents both the experimental and simulated performance of our rectifier when subjected to a steady-state inlet pressure. For a prediction of the asymmetry of an oscillatory input, the flow at equal but opposite input pressures can be compared, and we will use the term "pressure swing" to describe such a pair of pressures. The experimentally obtained flow bias for a pressure swing of 0.01 kPa is illustrated in Figure 2.3 by a pair of squared points; the evolution of the bias in the vicinity of zero pressure is shown in the insert. Finite element method (FEM) simulation results (Figure 2.3, vertically-tiled images at right) for a simplified two-dimensional rectifier of the same dimensions reveal that the bias is the result of differences in the velocity field for low and high inlet pressure swings. At low inlet pressure swings (1e-6 kPa), as in the case of the top two simulation images, the velocity field is dominated by viscous forces and is thus perfectly reversible. Conversely, for higher inlet pressure swings (1e-2 kPa), as in the case of the bottom two images, the velocity field is dominated by inertial forces and is highly asymmetric. Here, when vacuum is applied at the inlet, the resulting velocity field is more or less evenly divided among the three

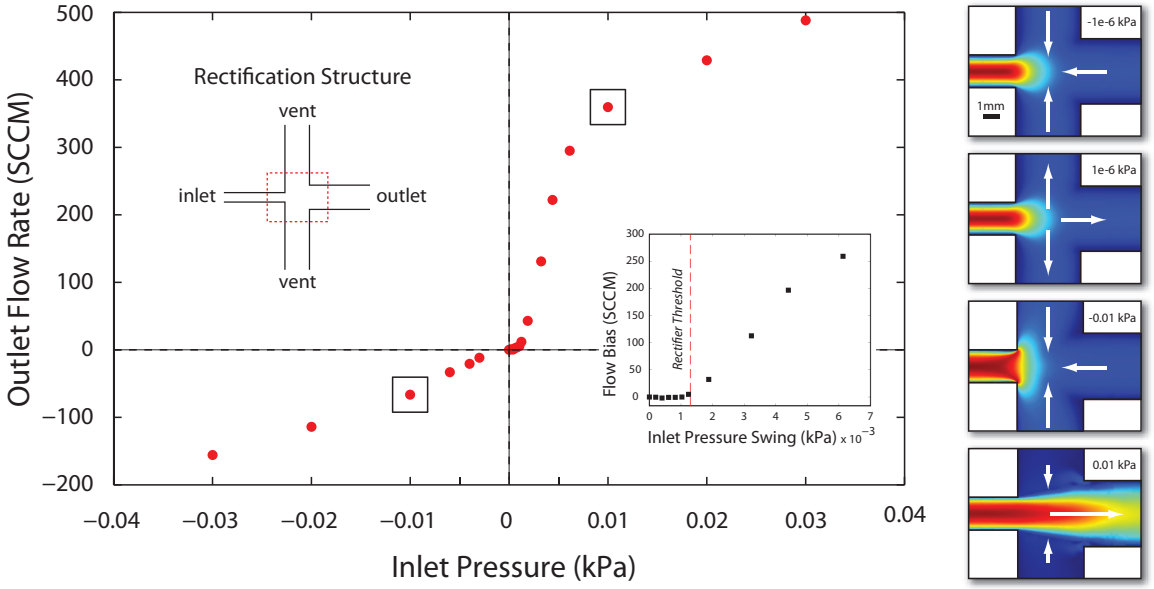


Figure 2.3: Rectifier outlet flow subject to ±0.03 kPa of inlet air pressure. (main plot) Experiment showing the resulting rectifier outlet flow rate over a range of inlet pressures. (inset plot) Evolution of rectifier flow bias computed as the difference in outlet flow rate at a given pressure swing. Bias at ±0.02 kPa represented as a pair of squared points. (inset schematic) Two-dimensional rectifier geometry used in FEM simulations. (images at right) Velocity field snapshots from FEM two-dimensional incompressible flow simulations. The top two images show the reversible viscous dominant flow field for extremely small inlet pressures ±1e-6 kPa. The bottom two images show the inertial dominant flow field at a pressure swing of ±0.01 kPa. Marked differences in the velocity field emerge due to flow separation and jetting at the rectifier inlet mouth.

remaining ports; however, application of a positive inlet pressure leads to the formation of a synthetic jet which extends from the mouth of the rectifier inlet toward the outlet. Application of a sinusoidally varying inlet pressure of sufficient strength then leads to a net unidirectional flow at the rectifier outlet. Thus the presence or absence of resonant tones allows us to jump between inertial- and viscous-dominated regimes thereby precisely controlling the state and level of each cavity output pressure.

### 2.2.3 Acoustically-Driven Liquid Motion

To illustrate the power of this concept for applications in microfluidic flow control, the device was connected to a polydimethylsiloxane (PDMS) chip with four parallel input channels each containing a 3 $\mu$L water droplet (Figure 2.4a). Prescribed sequences of resonant notes, each being responsible for the actuation of a single drop, were then used to selectively actuate droplets. Droplet velocity in response to the acoustic input signal is shown in Figure 2.4b. Acoustic input signals consisting of both single notes and chords produce instantaneous and targeted droplet motion, as shown in Figure 2.4b. To illustrate the speed at which instructions can be carried out, the tone durations in this experiment were kept brief ($\approx$0.2 sec) amounting to droplet displacements on the order of 0.2-0.5 mm per pulse. However, computerized waveform construction allows for full customization of the tonal input. Thus, a droplet can easily be moved over a longer distance or at a faster pace simply by adjusting the amplitude and duration of the corresponding wave component.

Although equal tone amplitudes of the input waveform do not produce uniform droplet velocities, the amplitude can easily be adjusted to compensate for this effect. In Figure 2.4, for example, with the audio amplifier set to output 7.92 V for an input wave amplitude of 1.0, the amplitudes resulting in the uniform movement of droplets A, B, C, and D were: 0.77 (404 Hz), 0.90 (484 Hz), 1.23 (532 Hz), and 1.42 (654 Hz), respectively. Increased voltage was necessary for higher frequency cavities because

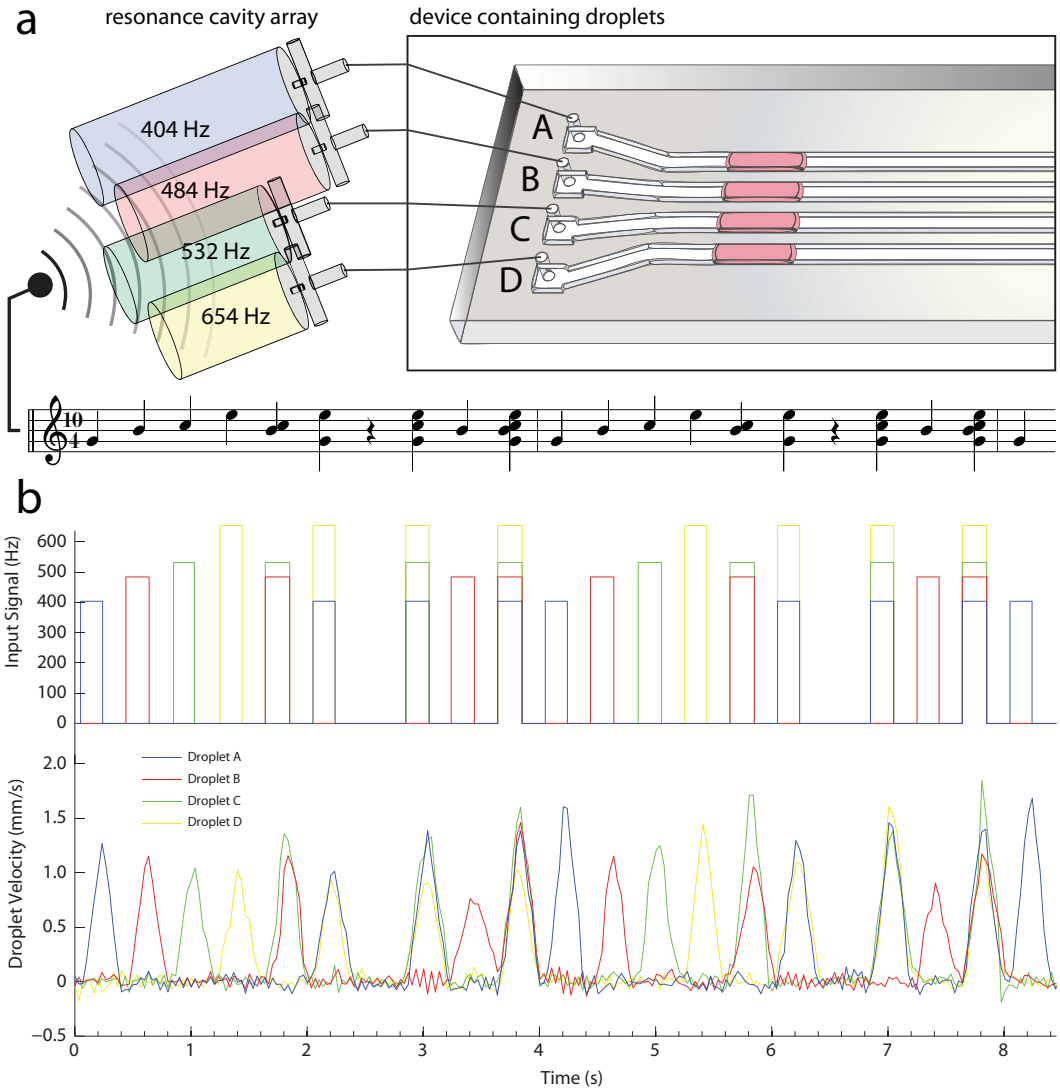


Figure 2.4: Multiplexed droplet motion. (a) Schematic representation of experimental setup depicting an input acoustic signal delivered to an array of resonance cavities, each of which is linked to an input on a microfluidic device (not to scale). (b) Input acoustic signal and resulting droplet velocity as a function of time illustrating programmed actuation of specific droplets in response to resonant musical tones supplied to the device. Chord amplitudes used to produce uniform droplet velocities were: B-C (0.89, 0.85), A-D (0.76, 1.39), A-C-D (0.80, 1.18, 1.25), and A-B-C-D (0.76, 0.76, 0.90, 1.25).

speaker diaphragm displacement, and as such, cavity output, is frequency dependent. In addition to the normalization of single tones, amplitudes were also adjusted within chords as early experiments exhibited a systematic enhancement of droplet velocity that appeared to be unique to each chord most likely due to frequency specific wave coherence. Amplitude multipliers unique to each chord were obtained, as in the case of single droplets, by monitoring droplet motion over many chord pulses. Despite efforts to ensure perfectly uniform droplet motion, however, variations of up to 20 % (on average) still exist due to fabrication inhomogeneities (Figure 2.4b).

To demonstrate the use of this scheme for the operation of more complex systems, the device was used to direct discrete drop motion within a network of pneumatically-coupled channels. In contrast to the parallel channel network shown in Figure 2.4, a branched network often necessitates the combination of multiple inputs to carry out a specific fluidic operation. Figure 2.5 illustrates how the four control inputs of the device were used to perform the standard fluidic unit operations of merging, mixing, transport, sorting, and splitting. To ensure precise operation, droplets were actuated in a pulsatile fashion, a strategy that is preferred when maneuvering one or more liquid slugs near a pressure node or junction. For example, during the splitting operation shown in Figure 2.5, the velocities of the two daughter droplets approximately double upon splitting. Use of continuous pressure control in this case would lead to a run-away of the resulting two slugs, a problem that is easily circumvented by shortening the timescale of the driving pressure. Conversely, for cases in which pulsatile control is not preferred such as for droplet transport over long distances or continuous flow operations, the device output can be readily converted to continuous operation.

In addition to propelling individual drops, the system we describe can also be used to pump continuous streams of fluid. Figure 2.6 illustrates how the device, when operated in continuous output mode, can be used to generate customizable acoustically-switchable concentration gradients. In the experiment, dynamically re-

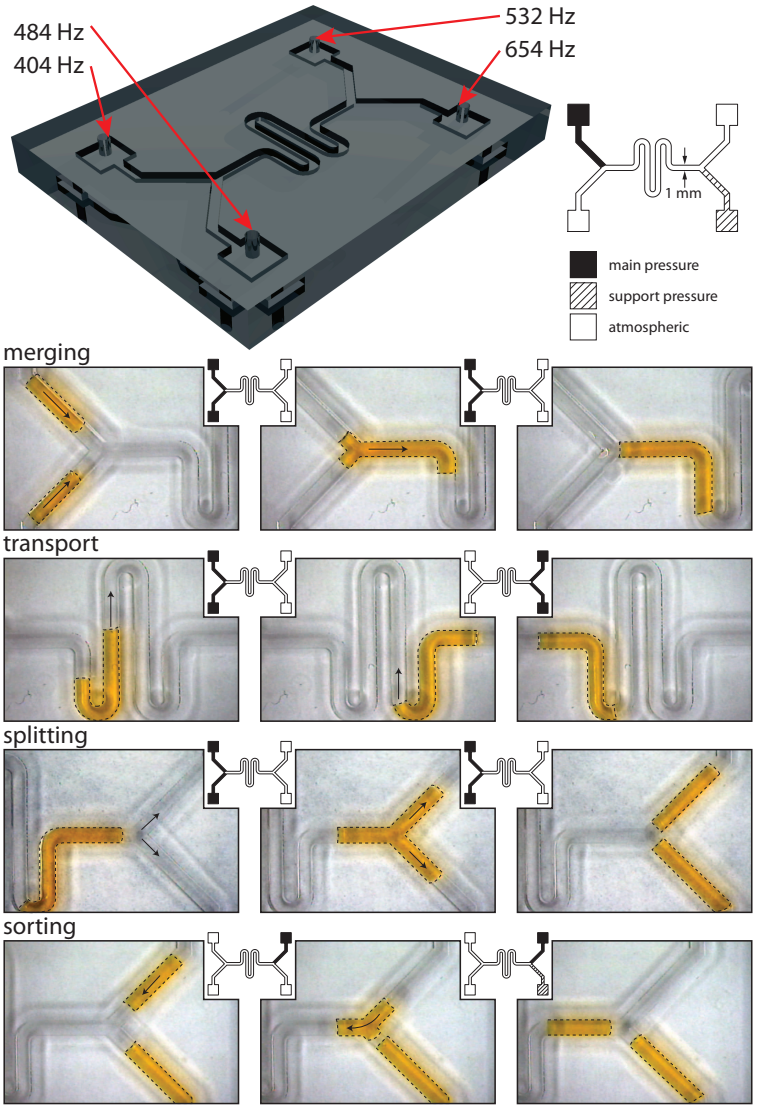


Figure 2.5: Performance of standard microfluidic unit operations using acoustically-controlled droplet motion. (top, left) schematic of branched channel PDMS device with associated cavity linkages (top, right) channel layout with legend illustrating the visual representation of three pressure states. *Main pressure* indicates areas where significant pressure is applied to induce droplet motion. *Support pressure* indicates areas where minimal pressure is applied to counter droplet motion. (bottom) Four sets of images depicting the standard fluidic unit operations of merging, transport, splitting, and sorting. Arrows on each image indicate ensuing droplet motion in response to acoustically-generated pressures (linking image).

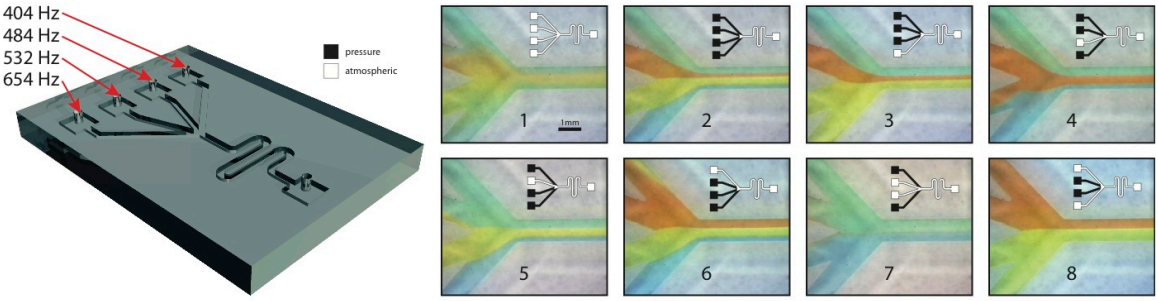


Figure 2.6: Acousticially-switchable gradient generation. (left) schematic representation of PDMS device used in gradient generation experiments. Resonance cavities are interfaced with the microfluidic device according to the frequencies listed. (right) A series of images depicting the state of the tonal input (image inset schematic) and the resulting liquid gradient that is produced. Cavity pressures were all tuned to ≈100 Pa.

configurable gradients are generated by connecting the device to four reservoirs of colored water and altering the strength and tonal composition of the acoustic output. When an acoustic signal is introduced, a gradient rapidly forms with a composition representative of the tones and amplitudes present (Figure 2.6: *images*, 2-8). For clarity, the output pressure of each cavity was set to the same value (≈100 Pa), however, fine-tuning of the component flow ratios is straightforward and involves a simple adjustment of the relative amplitudes of the input tones.

## 2.3 Materials and Methods

### 2.3.1 Device Construction

Device assembly is schematically represented in Figure 2.7. The acoustic source is a standard audio speaker (Pyle-PDMW6). The common air cavity was formed from a 0.155 m segment of 0.152 m ID thick-walled Pyrex. The cover plate was fabricated from a 0.155 m diameter, 0.01 m thick acrylic sheet. Four, 47 mm ID holes, for the cavity mounting ports were drilled in the cover plate along with five, 7 mm ID, vent holes for the minimization of pressure cross talk (Figure 2.7:*Cover Plate*). Four

resonance cavities were formed from 47 mm ID, 51 mm OD, borosilicate tube stock cut to 192 mm, 156 mm, 141 mm, and 111 mm, respectively. Cavities were sealed at one end, save for a small 2 mm ID, 10 mm long, borosilicate rectifier inlet port. Rectification structures consist of a 2 mm ID port which extends slightly into the confluence of a three-way cross formed by fusing three lengths of 4mm ID, 6 mm OD pyrex tubing (Figure 2.7: *Resonance Cavity/Rectifier*). All of the components in the final assembled device were joined using an off-the-shelf RTV silicone except for the rectification structure which was joined using a durable epoxy.

### 2.3.2 Measurement of Cavity Resonance

A constant voltage analog signal was generated using Labview (PCI-6031E) and amplified using a standard audio amplifier (Audiosource, AMP-100). In a typical experiment, the input waveform was steadily ramped from 300-800 Hz and the resulting output flow rate was monitored using a custom hot-wire anemometer and bridge circuit. Flow measurements were taken by placing the anemometer just proud of the rectifier outlet port and surrounding the assembly with a paper cylinder to minimize disturbance from ambient air currents.

### 2.3.3 Rectifier Flow Bias

For positive gauge pressures, air was delivered to the rectifier inlet using a mass flow controller (MKS, 11598B-05000SV). Application of negative gauge pressure was performed using a two-stage vacuum regulator in conjunction with a house vacuum source. In each case, the inlet pressure was monitored with a strain gauge (Omega, DP-25B-S) extending from a T-junction just prior to the rectifier inlet. Outlet flow rate was monitored using a custom hot wire anemometer and bridge circuit.

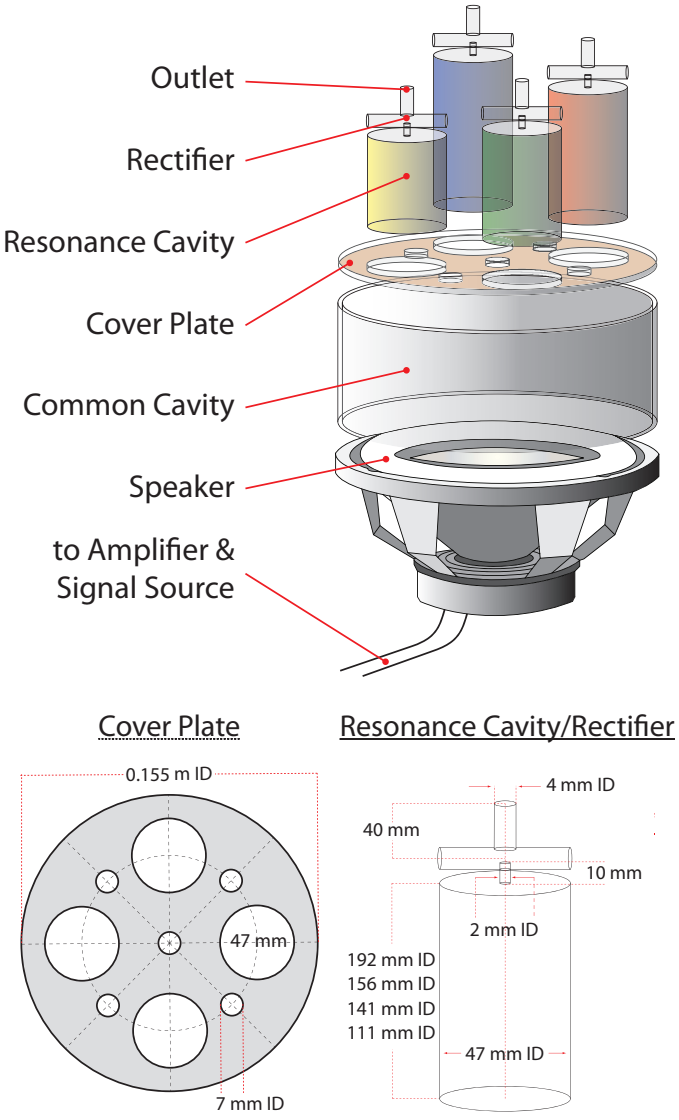


Figure 2.7: Device construction. (top) Exploded schematic view of device. (bottom) Detail of *Cover Plate* and *Resonance Cavity/Recitifer* with dimensions

### 2.3.4 Programmed Droplet Motion

Droplet experiments shown in Figures 2.4 and 2.5 were performed by coupling resonance cavity outlets to a nearby PDMS device using standard silicone tubing and syringe tip connections. The PDMS devices were fabricated using standard soft lithography protocols with 1000 $\mu$m wide by 500 $\mu$m deep channels. PDMS provides an ideal hydrophobic substrate on which to perform these experiments, as the non-wetting properties of the material eliminate the problems of droplet pullback and volume loss that accompany wetting surfaces. Prior to the experiment, a 3 $\mu$L colored water droplet was loaded into each channel using a micropipette. To induce droplet motion, computer-generated sequences of tones and chords with various amplitudes and durations were delivered to the device through a standard audio amplifier. The resulting droplet motion was captured using a stationary video post integrated into the optics of a stereomicroscope. Droplet velocities were later calculated from the video footage using a frame analysis algorithm.

### 2.3.5 Gradient Generation

The PDMS chip shown in Figure 2.6 was secured to the microscope stage and interfaced to the device using 4 mm ID silicone tubing. Gradients were generated by setting cavity output pressures to roughly 100 Pa and varying the combination of tones presented to the device. Reservoirs were created by filling a length of tube leading up to the device with dyed water. Both the reservoirs and the discharge line were fixed in level positions at the same height to eliminate hydrostatic driving pressures. The discharge line was fitted with a 1 mm ID plastic syringe tip cut to a shallow angle to minimize the pressure buildup associated with drop formation; however, periodic buildup and release of pressure associated with droplet formation at the outlet can still be seen during operation.

## 2.4 Conclusions

This work introduces a novel acoustic-based approach to distributed pressure control. In a process that can be likened to fiber optic communication, the device we have fabricated utilizes elements of acoustic resonance, fluidic rectification, and computer control in a simple arrangement to generate multiple, independently-addressable output pressures in the range of 0-200 Pa (control resolution of ≈10 Pa) that can be operated via a single control line. The device was interfaced to both droplet-based and continuous flow microfluidic systems and used to carry out various operations such as merging, transport, splitting, sorting, and on-demand gradient generation. Future devices may be scaled down and employ alternative methods of signal generation such as the direct displacement of a sealed cavity using piezoelectric transducers, or non-contact vibration of a flexible membrane using a remote acoustic source. Development of an on-chip equivalent to the device presented here could greatly simplify operation of complex lab-on-a-chip devices potentially extending the application base of such tools to non-scientists.

# CHAPTER III

# VARIED EFFECTS OF PHONONIC CRYSTAL LATTICE GEOMETRY ON THE EMERGENCE AND EVOLUTION OF TRANSMISSION BAND GAPS

## 3.1 Introduction

Phononic crystals represent an intriguing subclass of metamaterials whose physical structures have the capacity to shape acoustic transmission. Long known to exhibit band gap effects under certain circumstances, phononic crystal materials have garnered a good deal of attention recently because of their looming potential in the areas of vibration and noise-control [37–39], imaging [40, 41], RF communications [42], waveguides [43–45], and filters [46, 47]. Much of this recent popularity is also attributable to advances in microfabrication techniques, prior to which, the physical realization of phononic crystals was largely limited to macroscopic structures consisting of hand-assembled balls and rods [48–50]. The area of microfabricated phononic systems and devices is particularly interesting now, as researchers are developing methods to couple various device components (*e.g.*, CMOS circuitry, photonic crystals, and piezoelectrics) alongside phononic materials, creating an unprecedented level

of integration [51–53].

Traditionally, phononic crystals are binary composites possessing a periodic distribution of scattering centers; though some researchers have examined the potential utility of more complex hybrids [54]. Such composites can be solid/solid, fluid/fluid, or fluid/solid and typically consist of isolated scattering elements, or inclusions, embedded in a continuum host matrix [55]. Transmission gaps can be opened in these structures when the reflections sourced from a collection of individual scattering centers are in-phase — for plane wave propagation this is the Bragg or half wavelength resonance condition related to the spatial distribution of the inclusions along the polarization direction — thus forming a standing wave throughout the lattice which serves to reflect incident acoustic energy. In addition to the spatial periodicity of the crystal, inclusion shape has also been reported to influence gap formation [56]. The influence of inclusion shape is particularly significant at higher frequencies (acoustic wavelength comparable to inclusions dimensions) where multiple scattering effects become dominate. Surprisingly, while the vast majority of the literature is devoted to studying various criteria related to band gap formation, for these and other lattice properties, the exploration of the band gap effects related to the varied effects of lattice geometry has remained cursory.

In this work, we report on the influence of various geometric parameters as they pertain to the band gap properties of finite, two-dimensional phononic crystals. We discuss the utility of simplified analytical approximations as well as the analysis of phononic crystals in their infinite limit as tools for the modeling and interpretation of crystal transmission. The work is organized as follows: We first discuss the use of the finite element method (FEM) to simulate the transmission profiles of duct-confined two-dimensional (2D) phononic crystals subject to a variety of geometric perturbations of the crystal lattice. We then utilize a one-dimensional (1D) transfer matrix method approximation to model the location and contour of band gaps —

taking the view that the spatial periodicity of the 2D crystal, subject to plane wave excitation, is functionally equivalent to a 1D duct consisting of a series of rectangular constriction and expansion segments. Lastly, for comparison with the simulated 2D FEM transmission profiles, we compute band structures for the corresponding infinite phononic crystals and discuss their utility as tools for analyzing finite systems.

## 3.2 Theory

The base FEM simulation geometry examined in this work consisted of a 2D phononic crystal array confined within a semi-infinite duct in the x-y plane (Figure 3.1a). In each case, the y-dimension of the array, $n_y a_y$, was scaled as to completely span the transverse dimension of the duct ($n_y a_y \geq S_{duct}$), which was fixed at 1.0 cm. The longitudinal array width ($n_x a_x$), unless otherwise specified, was fixed at five columns of incusions ($n_x = 5$). The array itself was composed of cylindrical inclusions with semi-axis radii, $r_x$ and $r_y$, and spacing described by the pair of primitive lattice constants $a_x$ and $a_y$, as illustrated in Figure 3.1b. As a central point of discussion, we define as our base case geometry, the simple cubic arrangement shown in Figure 3.1b in which the lattice constants $a_x$ and $a_y$ are equal to 1000 $\mu$m or $a_{\text{base}}$, and the inclusion radii, $r_x$ and $r_y$, are equal to 250 $\mu$m or $r_{\text{base}}$. In the FEM model, we utilize the Helmholtz formulation of the elastic wave equation [57] and impose the rigid boundary condition for both the duct and inclusion walls. For the inlet and outlet duct boundaries, we imposed the radiation condition to ensure the absence of unwanted reflections. Additionally, at the inlet boundary we introduce a rightward traveling plane wave with pure x-polarization and unit amplitude. The elastic medium under consideration is air. Transmission profiles were generated by conducting a parametric sweep of the frequency domain (1kHz-1MHz) while simultaneously monitoring sound pressure levels at the inlet and outlet duct boundaries. The confining duct area being constant, intensity transmission coefficients were computed as the magnitude squared

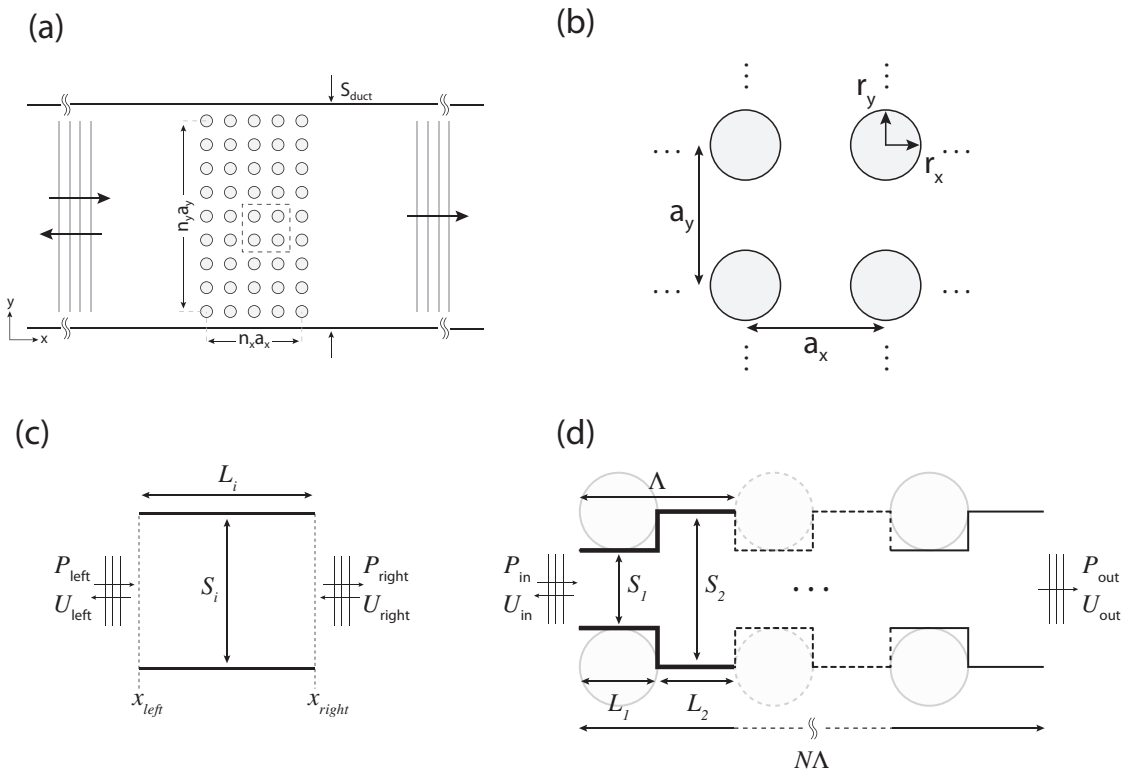


Figure 3.1: Simulation and model geometries: (a) FEM model system geometry consisting of a finite phononic crystal lattice composed of rigid cylindrical or elliptical inclusions confined to a semi-infinite rigid walled duct in the x-y plane. (b) Detail of phononic crystal lattice comprising rigid cylindrical inclusions with semi-axis radii $r_x$ and $r_y$ (for base case, $r_x = r_y = 250$ $\mu$m) and spacing defined by the lattice constants $a_x$ and $a_y$ (for base case, $a_x = a_y = 1000$ $\mu$m). (c) Generic duct segment used in the formulation of the TMM model (d) Schematic illustration of the 1D TMM approximation applied to an $N$ periodic lattice of period length $\Lambda$.

of the ratio of transmitted to incident amplitudes.

The transfer matrix method (TMM) — which relates the total pressure and volume velocity between two points in an elastic medium via a transfer matrix — is particularly useful for modeling the acoustic response of 1D periodic structures such as waveguides. Our utilization of the TMM is based on the assumption that, for plane wave propagation and $a_x$ polarization, the 2D array of inclusions shown in Figures 3.1a and 3.1b can be represented by a 1D duct consisting of rectangular constriction and expansion segments linked in series. Formulation of the TMM begins by solving

for the transfer matrix of a generic duct segment assumed to exist on the interval ($x_{left}$, $x_{right}$) as shown in Figure 3.1c. The total pressure at the left and right of this segment (neglecting viscous losses) can be described by the wave function

$$p(x,t) = P(x,t)e^{j\omega t} \tag{3.1}$$

where the spatial component of the total pressure at the duct extremities is an assumed superposition of rightward and leftward traveling waves

$$P(x,t) = \left\{ \begin{array}{ll} \hat{A}e^{jkx} + \hat{B}e^{-jkx} & (x < x_{left}) \\ \hat{C}e^{jkx} + \hat{D}e^{-jkx} & (x > x_{right}) \end{array} \right\} = \left\{ \begin{array}{l} P_{left} \\ P_{right} \end{array} \right\} \tag{3.2}$$

with complex amplitude coefficients $\hat{A}$, $\hat{B}$, $\hat{C}$, and $\hat{D}$, and $k = \omega/c$ is the wave number (where $\omega$ is the angular frequency and $c$ is the characteristic speed of sound in air). Application of the Euler relation to Eqn.3.2 and multiplying by the duct area, $S(x)$, the corresponding spatial component of the volume velocity is found to be

$$U(x,t) = \left\{ \begin{array}{ll} \frac{S(x)}{\rho_o c}\left(\hat{A}e^{jkx} - \hat{B}e^{-jkx}\right) & (x < x_{left}) \\ \frac{S(x)}{\rho_o c}\left(\hat{C}e^{jkx} - \hat{D}e^{-jkx}\right) & (x > x_{right}) \end{array} \right\} = \left\{ \begin{array}{l} U_{left} \\ U_{right} \end{array} \right\} \tag{3.3}$$

where $\rho_o$ is the ambient density of air. The total pressure and volume velocity at the duct boundaries can thus be represented by the matrix expression

$$\left( \begin{array}{l} P_{left} \\ U_{left} \end{array} \right) = \mathbf{T} \left( \begin{array}{l} P_{right} \\ U_{right} \end{array} \right) \tag{3.4}$$

where $\mathbf{T}$ is the transfer matrix whose components are related to the amplitude coefficients $\hat{A}$, $\hat{B}$, $\hat{C}$, and $\hat{D}$. Solving for the complex amplitude coefficients then gives the transfer matrix for a generic waveguide segment of length $L_i = x_{right} - x_{left}$, and

uniform duct area $S_i$

$$\mathbf{T} = \begin{pmatrix} \cos kL_i & j\frac{\rho_o c}{S_i}\sin kL_i \\ j\frac{S_i}{\rho_o c}\sin kL_i & \cos kL_i \end{pmatrix} \tag{3.5}$$

The total transfer matrix for a duct made up of multiple segments is obtained by concatenation of the individual transfer matrices. For example, the total transfer matrix of the N-periodic duct shown in Figure 3.1d would simply be

$$\begin{aligned} \mathbf{T}_N &= \left[ \begin{pmatrix} \cos kL_1 & j\frac{\rho_o c}{S_1}\sin kL_1 \\ j\frac{S_1}{\rho_o c}\sin kL_1 & \cos kL_1 \end{pmatrix} \begin{pmatrix} \cos kL_2 & j\frac{\rho_o c}{S_2}\sin kL_2 \\ j\frac{S_2}{\rho_o c}\sin kL_2 & \cos kL_2 \end{pmatrix} \right]^{N`} \\ &= \begin{pmatrix} T_{N11} & T_{N12} \\ T_{N21} & T_{N22} \end{pmatrix} \end{aligned} \tag{3.6}$$

where two individual transfer matrices from duct segments 1 and 2 comprise the 1D unit cell, with total period length $\Lambda$. As in Eqn.3.4, the pressure and volume velocity corresponding to the inlet ($P_{in}$, $U_{in}$) and outlet ($P_{out}$, $U_{out}$) of the N-periodic structure obey the matrix expression

$$\begin{pmatrix} P_{in} \\ U_{in} \end{pmatrix} = \mathbf{T}_N \begin{pmatrix} P_{out} \\ U_{out} \end{pmatrix} = \begin{pmatrix} T_{N11} & T_{N12} \\ T_{N21} & T_{N22} \end{pmatrix} \begin{pmatrix} P_{out} \\ U_{out} \end{pmatrix} \tag{3.7}$$

where the components, $T_{Nij}$, correspond to the amplitude coefficients of the total transfer matrix. The intensity transmission coefficient, assuming plane wave propagation, is proportional to the magnitude squared of the ratio of transmitted and incident amplitudes. Expanding the linear expressions in Eqn.3.7 and solving simultaneously, it can be shown that the intensity transmission coefficient is given by

$$\alpha_t = \left|\frac{P_{out}}{P_{in}}\right|^2 = \left|\frac{1}{\frac{1}{2}\left(T_{N11} + \frac{S_{out}}{\rho_o c}T_{N12} + \frac{\rho_o c}{S_{in}}T_{N21} + \frac{S_{out}}{S_{in}}T_{N22}\right)}\right|^2 \tag{3.8}$$

For comparison with the FEM transmission profiles of the 2D crystals, band structure calculations of the corresponding infinite phononic crystals were performed using the approach presented by Kuo *et al* [53]. In this method, unit cells of the crystal lattice are rendered and then tiled to infinity by application of periodic boundary conditions. Eigen frequencies contours of the first twenty propagating modes were then computed by sweeping the Bloch wave vector in reciprocal space along the high symmetry directions of the first irreducible Brillouin zone using a *Matlab* scripting routing interfaced with *COMSOL Multiphysics*.

## 3.3 Results and Discussion

### 3.3.1 Effects of Lattice Geometry

Altering the geometry of a phononic crystal can have dramatic and occasionally counterintuitive consequences on the locations and contours of transmission band gaps. Taking as a point of departure, the base case crystal lattice in Figure 3.1b, perhaps the most straightforward geometric alteration one can make is to vary the nearest neighbor spacing of the inclusions. Such a change amounts to parameterization of the two principal lattice constants, $a_x$ and $a_y$, which ultimately define the spatial periodicity of the system. Scaling of the unit cell in these principal directions augments the interference of incident waves and thus the location and contour of any transmission band gaps that may exist. Other changes to crystal geometry such as the scaling/reshaping of the inclusions or use of alternate lattice constructions are also possible and can figure heavily into shaping band gap properties. Longitudinal ($a_x$) contraction or expansion of a crystal unit cell, for example, primarily results in a marked shift in band center. The shift is most pronounced for, what will henceforth

be referred to as, the principal band gap, *i.e.*, the transmission band gap associated with the main period length of the crystal. The location of the principle gap — assuming sonification of the lattice with $a_x$ polarized plane waves as in Figure 3.1a — is described by the half-wavelength ($\lambda/2 = a_x$) condition, or Bragg length, as it is known in optics. FEM-simulated intensity transmission coefficients shown in Figure 3.2a show this migration of the principal band gap for several $a_x$ spacings relative to $a_{\text{base}}$. The gap center frequencies for $a_x/a_{\text{base}}$ equal to 0.6, 0.8, 1.0, 1.2, and 1.4, as predicted by FEM are, respectively, 259 kHz, 201 kHz, 165 kHz, 139 kHz, and 119 kHz. Interestingly, these predictions correspond to theoretical Bragg lengths ($\lambda/2 = c/2f$) that are slightly longer than the simulated dimensions (0.66, 0.85, 1.04, 1.23, and 1.44). This effective lengthening of the unit cell dimension $a_x$ arises due to the radiation impedance (mass-loading) that occurs at each change in area of the crystal. Such an impedance change gives rise to reflections which have a periodicity that is half that of the unit cell. Consequently, small band gaps open up at roughly twice the principal gap frequency. These gaps are fully resolvable only for relative spacings greater than unity as those below unity get lumped in with higher frequency multiple scattering effects, which begin at roughly 343 kHz (*i.e.*, where the wavelength is comparable to the inclusion diameter).

Transverse ($a_y$) contraction or expansion of the unit cell, by contrast, has a dramatic effect on the bandwidth and peak loss (minimum value of the intensity transmission coefficient at the gap center) of the principal band gap. Intensity transmission coefficients obtained for several transverse spacings, again relative to the base case ($a_y/a_{\text{base}}$), are shown in Figure 3.2b. We note that unlike altering the longitudinal dimension of the crystal unit cell, a change to the transverse spacing between inclusions has negligible effect on the frequency of the principal band center. This result is more or less expected, in view of the planar x-polarization of the incident phonons.

Before looking at the effect of bandwidth in Figure 3.2b, it is helpful to consider

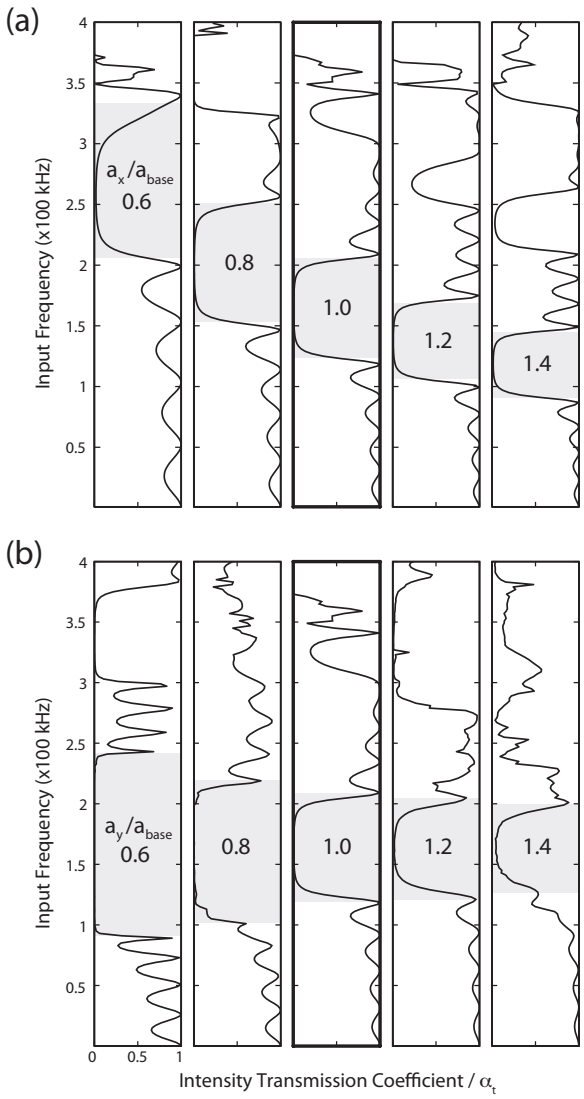


Figure 3.2: FEM transmission profiles highlighting the location and contour of the principal band gap (shaded regions) subject to (a) longitudinal and (b) transverse modifications to the crystal unit cell. Spacing reported relative to base lattice dimensions (outlined in bold).

the limiting cases. Extremely large vertical spacing ($a_y/a_{\text{base}} \gg 1$), for example, represents the limit of perfect transmission; that is, the magnitude of the interference provided by the inclusions, when spaced very far apart, goes to zero and incident phonons at all frequencies are transmitted without attenuation. Extremely small vertical spacing (limit as $a_y/a_{\text{base}} \to 0$), on the other hand, represents the limit of zero transmission. In this case, the rigid inclusions form a continuum, akin to a solid wall, which rejects all incident acoustic energy. The profiles in Figure 3.2b illustrate the intermediate region between these two limiting cases within which the incident phonons are transmitted with some degree of attenuation and the bandwidth of the principle gap scales inversely with the transverse spacing of the inclusions. At a relative vertical spacing of 1.4, the principal gap, though prominent, is narrow in bandwidth (76 kHz) and incomplete with a peak loss of 5e-2. At the lower end, for a relative vertical spacing of 0.6, the principal gap bandwidth is significantly larger (154 kHz) and the gap is essentially complete, with a peak loss of approximately 5e-5 — a three orders of magnitude reduction in intensity for roughly a 2x change to the transverse spacing.

Apart from a scaling of the unit cell, inclusion size and shape can also heavily influence the gap properties of phononic crystals. Recent work exploring the transmission effects of substituting different inclusion shape classes such as triangles, squares, hexagons, *etc.*, have been reported [56]. It is found that the broadest and deepest band gaps occurred when inclusion geometry most closely mimicked the parent lattice structure. We chose to explore inclusion anisotropy effects by altering the longitudinal eccentricity of the cylindrical inclusions, *i.e*, varying the aspect ratio of the semi-axis radius $r_x$, while holding $r_y$ and the base case unit cell dimensions fixed. Figure 3.3 shows the resulting FEM transmission profiles for normalized inclusion aspects ratios ($2r_x/a_{\text{base}}$) from 0.1 to 0.9, where an aspect ratio of 0.5 corresponds to the neutral or base case. We find that the principle gap center, peak loss, and bandwidth are sym-

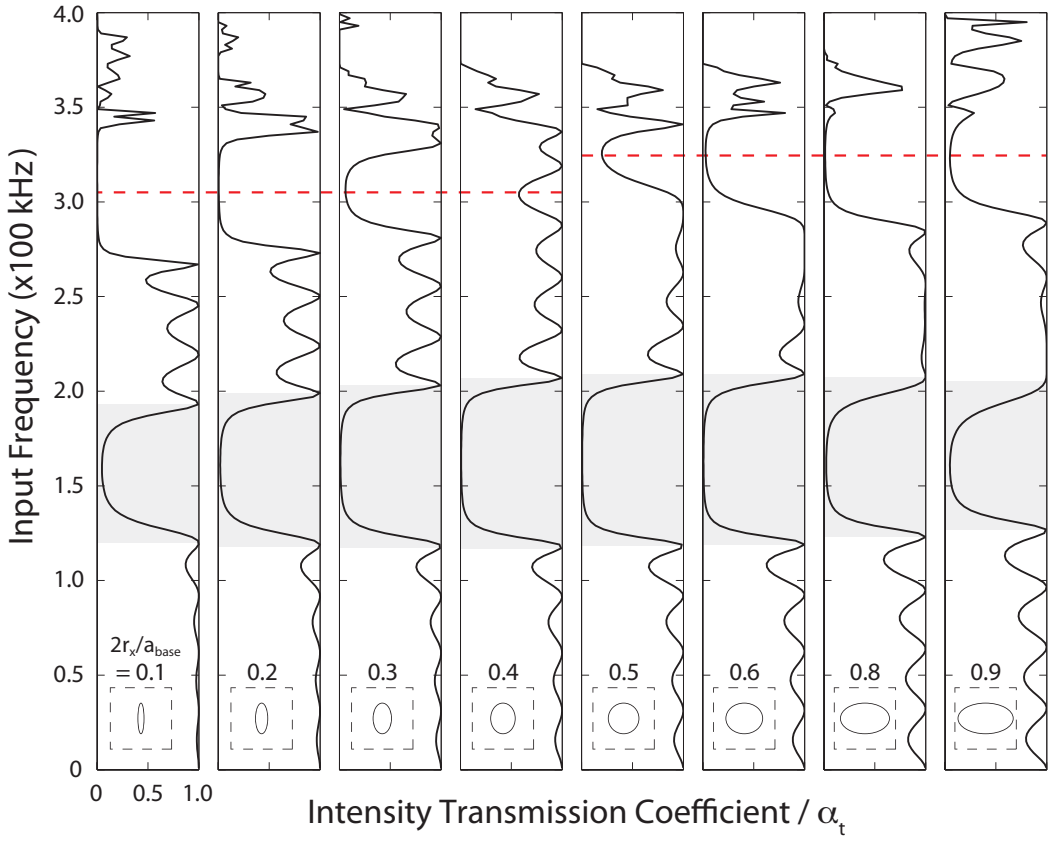


Figure 3.3: FEM transmission profiles detailing the effect of inclusion $x$-eccentricity (insets) on the location and bandwidth of the principle band gap (shaded rectangles) as well as the break in symmetry of the mass loading gap (dashed lines).

metric about a neutral inclusion aspect ratio. This intriguing symmetry, we suspect, occurs due to an inversion of the periodic structure. That is, for pairs of inclusion aspect ratios equidistant from the base case, the relative fractions of the unit cell width $a_x$ that are occupied inclusion and air-space (respectively, the constriction and expansion segments of a 1D waveguide approximation) are switched thus preserving the overall longitudinal periodicity of the system.

Inversion of the periodic structure does not, however, produce entirely equivalent transmission profiles. This is particularly evident for the secondary gaps associated with mass-loading at approximately 320 kHz, whose contours significantly change over the values sampled (Figure 3.3, dashed line). Apropos, we can make two immediate

observations with regard to the mass-loading gaps. First, the magnitude of the mass-loading dip increases away from an inclusion aspect ratio of 0.4. Second, there is an apparent shift in the location of the gap center frequency between the inclusion aspect ratios 0.4 and 0.5. Qualitatively, we can understand the second observation by looking at the length scales over which the radiation impedance occurs. For inclusions that are highly compressed in their x-aspect ($2r_x/a_{\text{base}} = 0.1$), for example, the change in area is very abrupt — occurring over just 10% of the total unit cell width ($a_{\text{base}}$) — corresponding to radiation impedance with a spacing that is 90% of the total unit cell width. Oppositely, for elongated inclusions the impedance occurs over 90% of the unit cell width with a spacing of the impedance of 10%. The difference in the periodicity of the impedance, we suspect, accounts for the frequency shift observed though the authors are perplexed as to why shift is stepwise instead of gradual. Regarding to the first observation, the apparent minimum in the magnitude of the radiation impedance at 0.4 rather than 0.5 is a consequence of the effective length corrections discussed above. Specifically, the true minimum occurs where the periodicities of the waveguide and the impedance match (theoretically 0.5); but the effect of mass-loading forces this condition slightly down in frequency.

With regard to unit cell filling fraction (FF), the observed effect on the principal band gap depends on the manner in which it is changed. Commonly, FF is augmented via uniform scaling of the inclusions and/or unit cell. To probe for geometric path-dependent effects, we modify FF in four distinct ways (Figure 3.4a). In Figure 3.4b and 3.4c, we show the change in both bandwidth and peak loss of the principal gap for FFs obtained by: (1) isotropic scaling of the inclusion radii, (2) alteration of the $x$-eccentricity of the inclusions, and (3-4) stretching the unit cell dimensions in both the longitudinal and transverse directions. The data reflecting the change to the bandwidth (Figure 3.4b) exhibits trajectories of two distinct magnitudes. The shallower of the two trajectories relates to geometric modification of the inclusions,

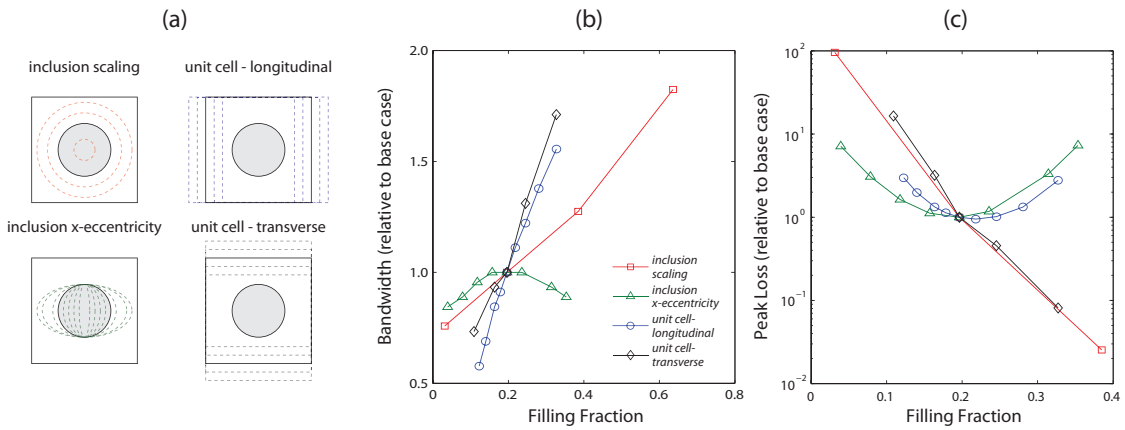


Figure 3.4: Influence of filling fraction ratio (FF). (a) Schematics detailing the four geometric paths taken in the modification of the FF. (b) Bandwidth (normalized to base case) of the principal band gap as a function of FF. (c) Peak loss of the intensity transmission coefficient (normalized to base case) of the principal band gap as a function of FF.

and the steeper of the two, to changes in the unit cell dimensions. Not surprisingly, in the vicinity of the principal gap, changes in the unit cell dimensions ($a_x$ and $a_y$) exhibit the stronger dependence — a result of the changing Bragg length mentioned above. Only at higher frequencies (wavelengths comparable to the inclusion dimensions, $\lambda/2 \leq 2r$), where multiple scattering effects become dominant, would changes to inclusion geometry begin to compete with unit cell effects. Approximately linear trajectories are observed in each case, save the parabolic trajectory associated with inclusion eccentricity. This parabolic contour is tied to the inversion of the periodic structure mentioned above.

For peak loss, the division of trajectories occurs instead between longitudinal and transverse modifications to the crystal geometry — though arguably the scaling of inclusion radius in this case qualifies as both. Peak loss (Figure 3.4c) values obtained for isotropic scaling of the inclusion radius and transverse lattice spacing decreases exponentially for successively larger FF. Qualitatively, this observation can be understood by considering that an increase in FF via these parameters yields geometries that increasingly resemble a solid wall. More interesting though, are the parabolic

contours associated inclusion eccentricity and longitudinal spacing. Qualitatively, the best peak loss is achieved when the amplitude of the standing wave in the gap region is strongest. Physically, this situation occurs near the base case (FF=0.2), where reflections from all perturbations in the waveguide are in phase, *i.e.* when the inclusion width is exactly one half of the total period length.

Interestingly, use of alternate lattice constructions does not guarantee unique band gap properties. For example, the principal gap profiles obtained for the square to rhombic lattice transformation are essentially insensitive to the geometric reconstruction. Figure 3.5a shows the transmission profiles of the base case to rhombic transformation, which is accomplished by introducing a vertical shift ($y_{shift}$) between consecutive columns of inclusions, as illustrated in Figure 3.5b. That this oblique character does little in the way of effecting the location and contour of the principal band gap is somewhat counterintuitive, as one might expect the staggered arrangement of inclusions to reject a greater fraction of incident acoustic energy relative to the base case. However, in the vicinity of the principal gap—where only plane waves propagate and the acoustic wavelength is long compared to the array spacing— the impedance characteristics of a single air aperture will behave identically to that of two smaller apertures of the same length and equivalent total area operating in parallel (Figure 3.5c). Thus, the transmission profiles measured on the other side of the crystal slab are blind to the geometric transformation of the lattice. This reasoning of course does not apply at high frequencies or in cases where damping is especially prevalent. Another interesting facet of this transformation is the extinction of the mass-loading gap. As mentioned above, this peak forms as a result of the mass-loading at each change in area of the modulated structure, effectively introducing an additional periodicity into the system and thus an additional excitable resonance. Decay of this peak as well as the increase in noise likely occurs because the vertical shifting of the crystal into non-symmetric arrangements introduces destructive interference

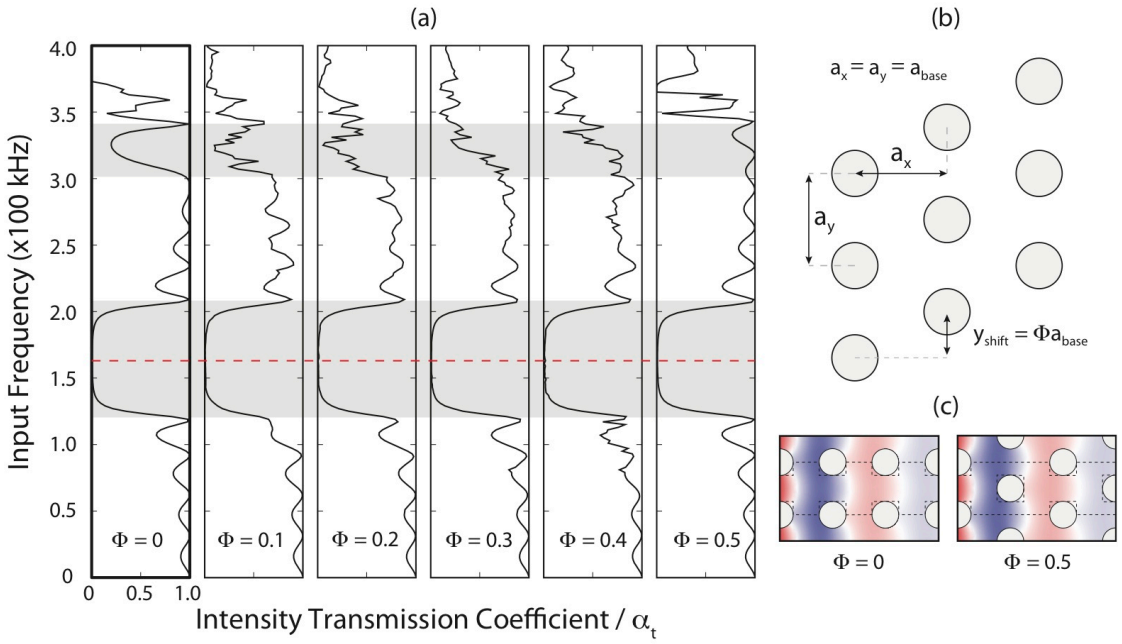


Figure 3.5: FEM transmission profiles highlighting the rhombic transformation of the base case lattice. (a) Simulated profiles reflecting a steady rhombic transformation of the base case lattice. (b) Schematic illustration of the transformation, performed by introduction of vertical shift ($y_{\text{shift}} = \Phi a_{\text{base}}$) between consecutive inclusion columns. (c) Pressure field images from FEM for $\Phi = 0$ and $\Phi = 0.5$.

thus eliminating the resonance associated with the radiation impedance.

### 3.3.2 Analytical Modeling

Full-fledged phononic crystal simulations are computationally intensive and challenging to implement. We employ a 1D TMM model for predicting phononic crystal transmission, a computationally leaner alternative which, despite its simplicity, capably reproduces the 2D FEM principal gap profiles for all of the geometric parameters sampled here. To serve as a base for comparison, we initially seed our TMM model with the FEM-simulated dimensions corresponding to the base case lattice. The resulting 1D unit cell, shown in Figure 3.6a, is constructed from two duct segments: (1) a constriction segment of length, $L1$, and width, $S1$, which corresponds to the aperture between vertically neighboring inclusions and (2) an abrupt expansion segment

of length, $L2$, and width, $S2$, which corresponds to the air-space between consecutive inclusions in the x-direction. The total period length of the unit cell is $\Lambda$. Calculated TMM transmission profiles for crystals with varying thickness ($n_x = 1, 2, 3, 5, 7, 9$) predicted using these simulated dimensions are plotted in Figure 3.6c alongside the full 2D FEM simulations results of the base case.

Use of the "as-simulated waveguide dimensions clearly results in over prediction of peak loss, bandwidth and, to a lesser extent, band center of the principal gap. The primary sources of these over predictions are likely: (1) error inherent to the geometric approximation, *i.e.*, modeling a cylindrically modulated duct with abrupt rectangular segments and (2) mass-loading or radiation impedance. The latter can be corrected for in the model, as discussed above, by adding length to the simulated constriction ($L1$). To rectify the former, we modified the constriction width ($S1$) to offset the error in the geometric approximation. Assuming no change to the expansion segment, the resulting waveguide, with new effective constriction dimensions ($L1_{\text{eff}}, S1_{\text{eff}}$, and $\Lambda_{\text{eff}}$) is shown in Figure 3.6b. Effective constriction dimensions which produced the most reasonable fits to the FEM data in Figure 3.6c were, $L1_{\text{eff}} = 555$ $\mu$m or $1.11(L1)$ and $S1_{\text{eff}} = 725$ $\mu$m or $1.45(S1)$. The width ($S1_{\text{eff}}$) being nearly 50% larger than its as-simulated value is reasonable considering that the constriction width is at the base case dimension only at the point of tangency and elsewhere flares to twice this width over the remaining constriction length. The effective length correction of approximately 50 $\mu$m, on the other hand, is close to the theoretical Bragg lengths alluded to earlier.

The effective constriction dimensions obtained from the base case arrangement cannot be applied as a universal correction. In fact, we found that a unique set of effective dimensions was needed for each of geometric perturbation sampled. Fortunately, the act of searching for suitable effective corrections provides insight that can help to rationalize the FEM predictions. Moreover, successful reproduction of the

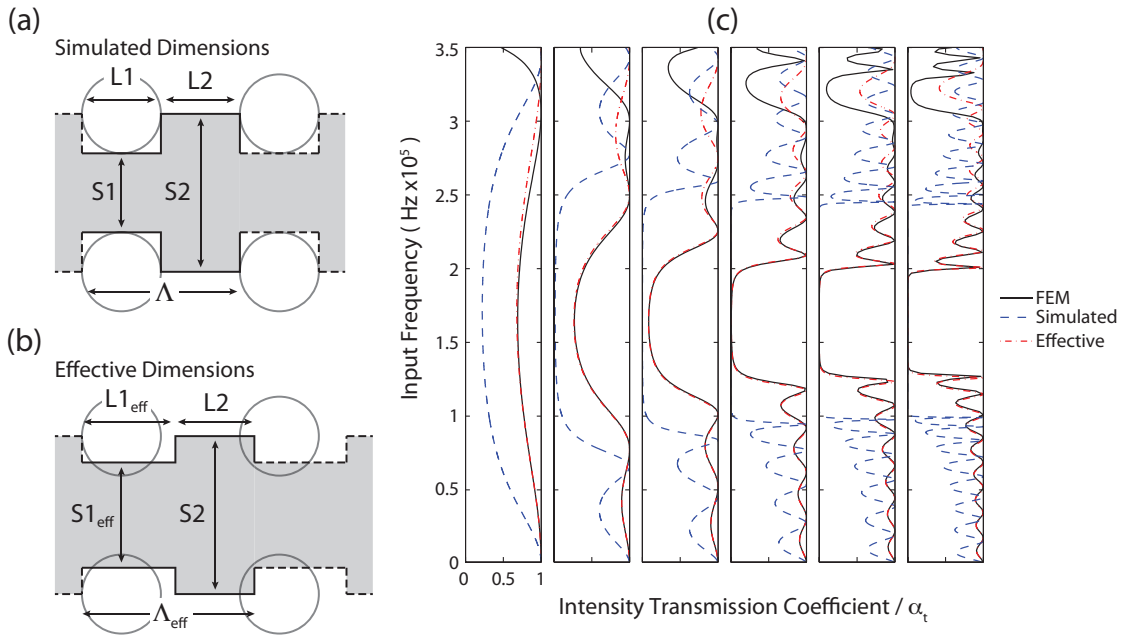


Figure 3.6: Transfer matrix (TMM) model results for crystals of varying thickness. (a-b) Schematic of simulated and effective 1D waveguide dimensions used in TMM model. (c) Transmission profiles for duct-confined phononic crystals of varying thickness (left to right, $n_x = 1, 2, 3, 5, 7, 9$) as predicted by FEM (solid black curves). TMM model results based on simulated (dashed blue curves) waveguide dimensions ($L1, S1, L2, S2$) and effective (dashed red curves) waveguide dimensions ($L1_{\text{eff}}, S1_{\text{eff}}, L2, S2$).

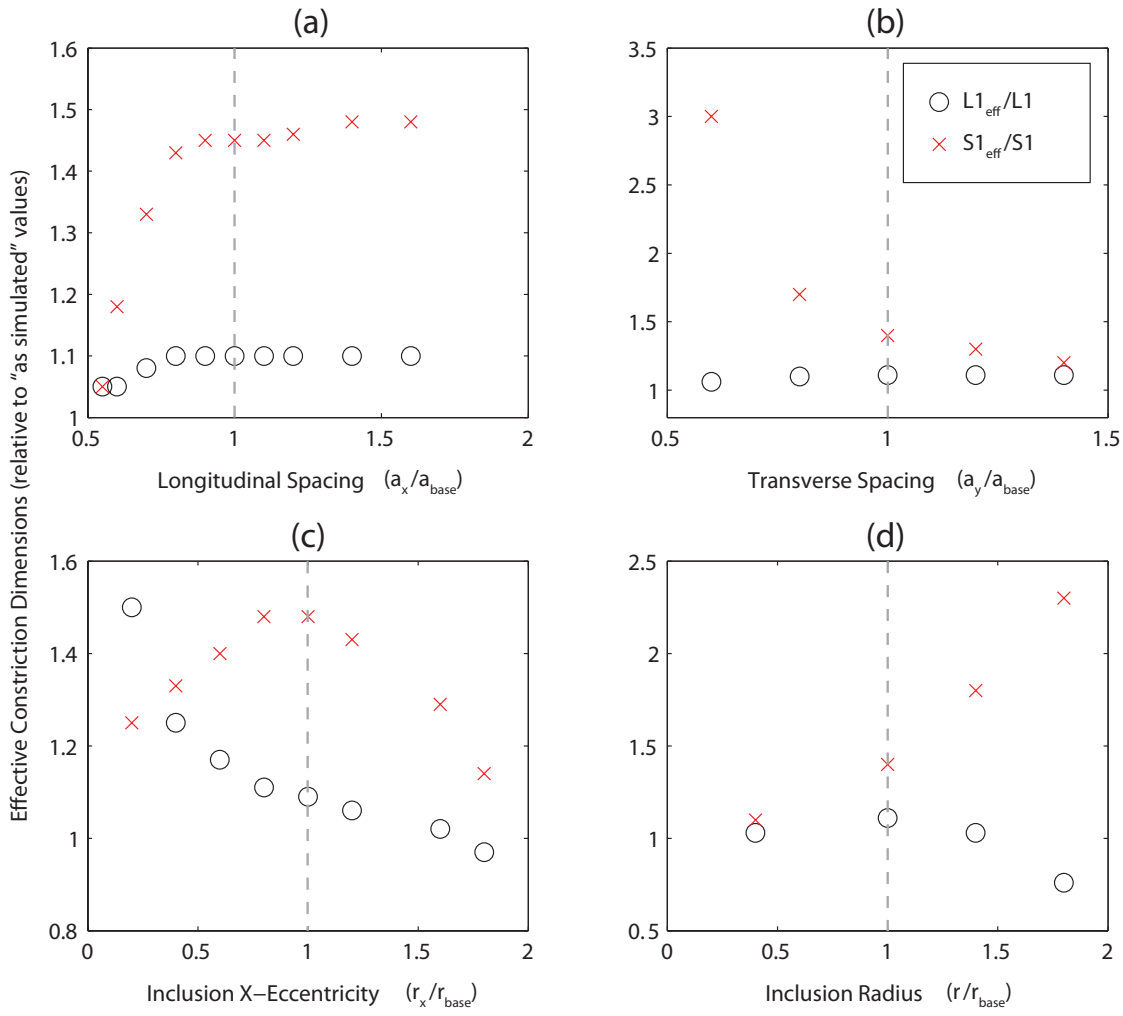


Figure 3.7: Effective constriction dimensions relative to as simulated values. (a) longitudinal spacing relative to $a_{\text{base}}$, (b) transverse spacing relative to $a_{\text{base}}$, (c) inclusion $x$-eccentricity relative to $r_{\text{base}}$ (d) inclusion radius relative to $r_{\text{base}}$.

FEM profiles indicates that we may analyze the transmission properties of complex 2D crystals within the framework of simple 1D waveguides, which are intuitively more tractable. The effective constriction parameters for each of the geometric alterations of the lattice discussed so far are shown in Figure 3.7.

The required effective corrections corresponding to longitudinal contraction of expansion of the unit cell are shown in Figure 3.7a. Relative longitudinal spacings — achieved by varying the $L2$ dimension of the 1D unit cell — less than unity ($a_x < a_{\text{base}}$), the normalized effective constriction dimensions, expressed as the ratio

of the effective to simulated dimension ($L1_{\text{eff}}/L1$ and $S1_{\text{eff}}/S1$), approach the limit corresponding to no correction or unity on the ordinate axis (Figure 3.7a). The decline in the required correction for tighter longitudinal spacing reflects the disappearance of expansion segment $L2$, or more simply, the waveguide increasingly resembles an unperturbed 1D duct. For spacing greater than unity, the effective constriction dimensions, as one might expect given that the aspect ration of the constriction is non-changing, become insensitive to changes in longitudinal spacing, leveling off near the effective dimensions obtained for the base case ($L1_{\text{eff}}/L1 \approx 1.1$, and $S1_{\text{eff}}/S1 \approx 1.45$).

Unlike the longitudinal case, changing the transverse spacing ($S1$) represents an actual modification to the aspect ratio of the constriction. The effective constriction dimensions obtained for transverse spacing are plotted in Figure 3.7b. We see that for large transverse spacing ($a_y > a_{\text{base}}$), the width correction ($S1_{\text{eff}}/S1$) approaches unity, whereas, for small spacing ($a_y < a_{\text{base}}$) it grows to nearly three times the base case constriction dimensions. Interestingly, the absolute difference in the effective and theoretical constriction widths is approximately constant at $214 \pm 13$ $\mu$m. This difference, remaining essentially constant, is reasonable given that the cylindrical profile of the inclusions — that intuitively should dictate the width correction — is not changing here. Moreover, this fixed correction accounts for the observed trend in the normalized effective width ratio, which grows rapidly for small transverse spacing and approaches unity for arbitrarily wide constrictions. The effective constriction length follows a trajectory that is nearly identical to the longitudinal case. This is unexpected as effective length corrections for macroscopic flaring horns are typically proportional to duct width.

The results for inclusion $x$-eccentricity are slightly more complicated (Figure 3.7c). The effective constriction width correction, for example, is parabolic with the maximum correction occurring near the base case ($r_x/r_{\text{base}} = 1$). We speculate that this is the result of the inclusions being more geometrically accurate to their rectangu-

lar approximations at the extremes. In the lower limit ($r_x/r_{\text{base}} < 1$), for example, inclusions are highly compressed in their x-aspect and, as such, accurately resemble an abrupt rectangular constriction with near vertical walls. Likewise, in the opposing limit where the inclusions are elongated in their x-aspect, the periphery of the inclusion reasonably follows that of a long constriction. The intermediate aspects, however, are not as close in their impression of the rectangular waveguide segments and thus require greater width corrections. It is helpful to separately analyze the effective length corrections in two parts. Below the base case ($r_x/r_{\text{base}} \leq 1$), the absolute length correction required remains constant at 48 $\pm$ 3 $\mu$m. This is in keeping with the relative constancy of the gap center frequency shown in Figure 3. However, when normalized to the base case, the increasing $r_x$ dimension of the inclusions produces a rapid decline of $L1_{\text{eff}}/L1$ toward unity, *i.e.*, the condition reflecting no correction. For values above the base case (namely, $r_x/r_{\text{base}} = 1.20, 1.60, \text{and} 1.80$), we find the required length corrections to be 35 $\mu$m, 16 $\mu$m, and (-23 $\mu$m), respectively. The fact that the correction appears to become negative is perhaps reasonable if we consider: (1) the geometric resemblance mentioned earlier for highly elongated inclusions should decrease the required correction, and (2) elongated flaring horns, such as those found in wind instruments, have been shown to exhibit negative effective length corrections.

Scaling of the inclusion radius represents the situation in which both constriction length and width vary simultaneously and opposite to one another (Figure 3.7d). That is, for large radii the constriction is long and narrow whereas for small radii the constriction is short and wide. It is important to note that with fixed base case lattice spacing, adjustment of the inclusion radius is constrained to a dimensionless inclusion radius ($r/r_{\text{base}}$) equal to a value of two. At this limit, the inclusion diameter is equal to the unit cell width and the rigid inclusions form a continuum akin to a solid wall. Near this limit, the width correction increases rapidly — analogous to the narrowing

of the transverse spacing in Figure 3.7b. By contrast, the length correction decreases in the neighborhood of two eventually dropping below one, indicating a negative length correction. This result is consistent with the negative correction observed for the highly elongated inclusions in Figure 3.7c. An inclusion radius of zero, on the other hand, corresponds to the physical limit in which the inclusion vanishes and the waveguide becomes an unperturbed channel with width $S2$. From Figure 3.7d, we observe that both the effective length and width corrections approach unity in the limit where the inclusion radius vanishes. This represents the unperturbed channel case in which $S1_{\text{eff}}$ approaches $S2$ and $L1$ approaches zero.

### 3.3.3 Band Structure Calculations

Study of phononic crystal gap formation in the infinite limit can provide significant insight — particularly at higher frequencies where plane wave methods are no longer valid — into the analysis of finite systems. Take, for instance, the base case FEM transmission profiles for crystals of varying thickness ($n_x = 3, 5$, and 9) shown in Figure 3.8 (right panel) and the corresponding $\Gamma - \text{X}$ band structure Figure 3.8 (left panel). The simulated profiles exhibit five distinct gap regions, beginning with the principal gap at 165 kHz, where acoustic transmission is severely attenuated. Remarkably, these gap regions correspond, at least in the case of the principal and mass-loading gaps (labeled 1 and 2), to regions in the band structure where no propagating modes are predicted to exist. Furthermore, the predicted gap locations and gap widths appear to converge for crystals with as few as nine periodic repeats. Such agreement bolsters the notion that band structure calculations can be used in the analysis of finite systems

Interestingly, the higher frequency band gaps (labeled 3, 4, and 5) are not predicted in the band structure due to the presence of extraneous modes (Figure 3.8, dashed curves) that traverse the anticipated gap regions. These modes form as a result

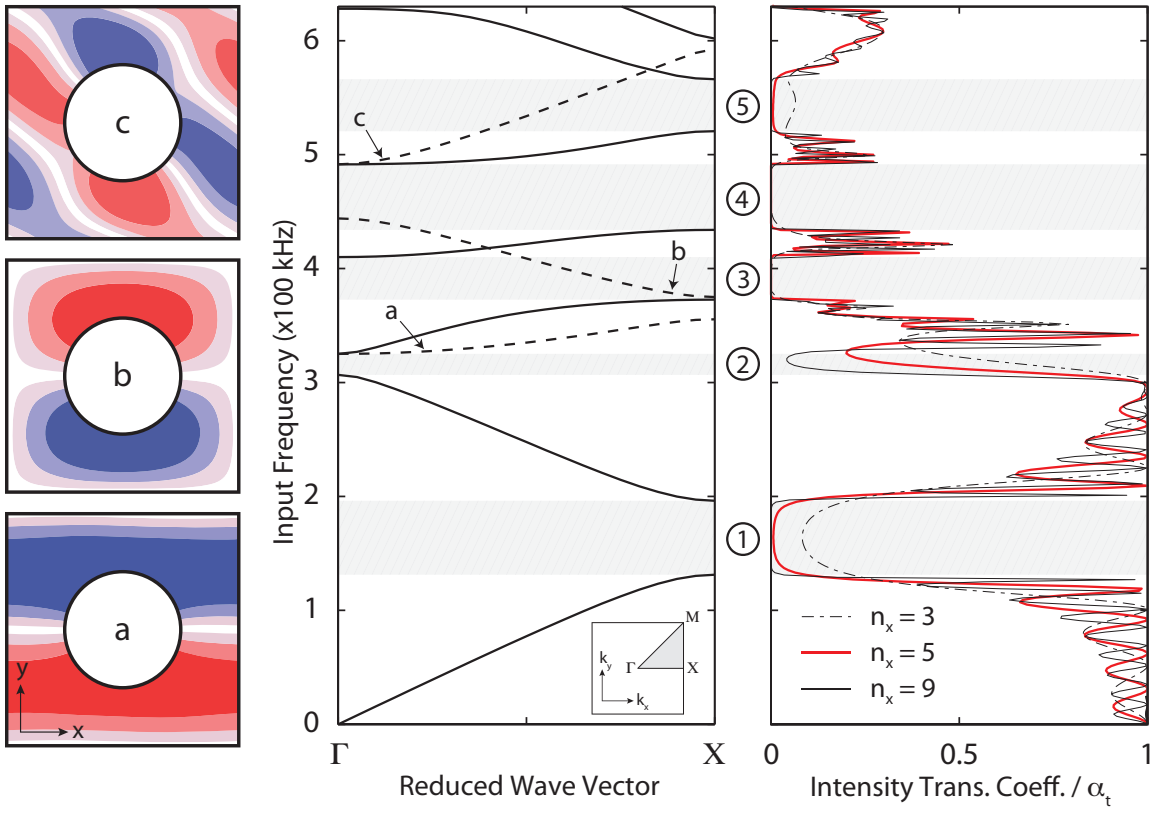


Figure 3.8: Calculated band structure and simulated (FEM) transmission profiles for base case crystals of varying thickness. (Center panel) $\Gamma - \mathrm{X}$ band structure calculated along the $k_x$ direction of the first irreducible Brillouin zone (inset) showing the location of observed transmission gaps (hatched rectangles) as well as the location of transverse modes (a, b, and c: pressure field images at left). (Right panel) Simulated FEM transmission profiles of base lattice crystals ($n_x = 3, 5$, and 9 periods thick) highlighting the evolution of gap width and location with increasing thickness.

of degenerate Eigen solutions (multiple geometric orientations at a single frequency that satisfy the wave equation) which, due to their transverse character, are not (or are only weakly) excited by the longitudinally-polarized incident waves. Transmission profiles obtained from FEM are thus "deaf" to these modes, leading to the observation of gaps 3, 4, and 5. For visual inspection, pressure fields for these transverse degenerates are plotted in Figure 3.8 (images a, b, and c at left). Similarly, pressure fields for every band in Figure 3.8 is shown in Figure 3.9.

Band structure calculations were then validated by comparing the predicted pressure fields at the gap edges to the FEM simulations of the duct-confined crystals. This comparison was done utilizing the transmission data for five rows of inclusions ($n_x = 5$), as shown above in Figure 3.8. It is worth noting that the selection of the $n_x = 5$ data is not significant and that the same comparison could be performed with an alternate number of periodic repeats. The results, for the first three band gaps are plotted in Figure 3.10 (see supplemental information for the complete result featuring all 5 gaps). From Figure 3.10, we see that the modes at the gap edges predicted for the infinite phononic crystal are indeed present in the pressure fields of the finite duct confined systems. However, due to the finite scale of the crystal, the locations of the band gap edges and the gap center frequency in the finite case are slightly greater than the values obtained for the infinite crystal — a disparity that resolves for larger values of $n_x$.

Non-homogeneities in the pressure field — as seen in the FEM snapshots of the simulated crystals in Figure 3.10 — are also apparent and likely emerge due to a combination of reflections from the duct walls as well as weak excitation of transverse and/or higher energy modes. Furthermore, the exact location of the target band structure modes within the finite crystal appears to vary along the x-dimension of the array (compare, for example, the FEM snapshots of the lower gap edges of band gaps 2 and 3 in Figure 3.10). This variability, we suspect, relates to the particular

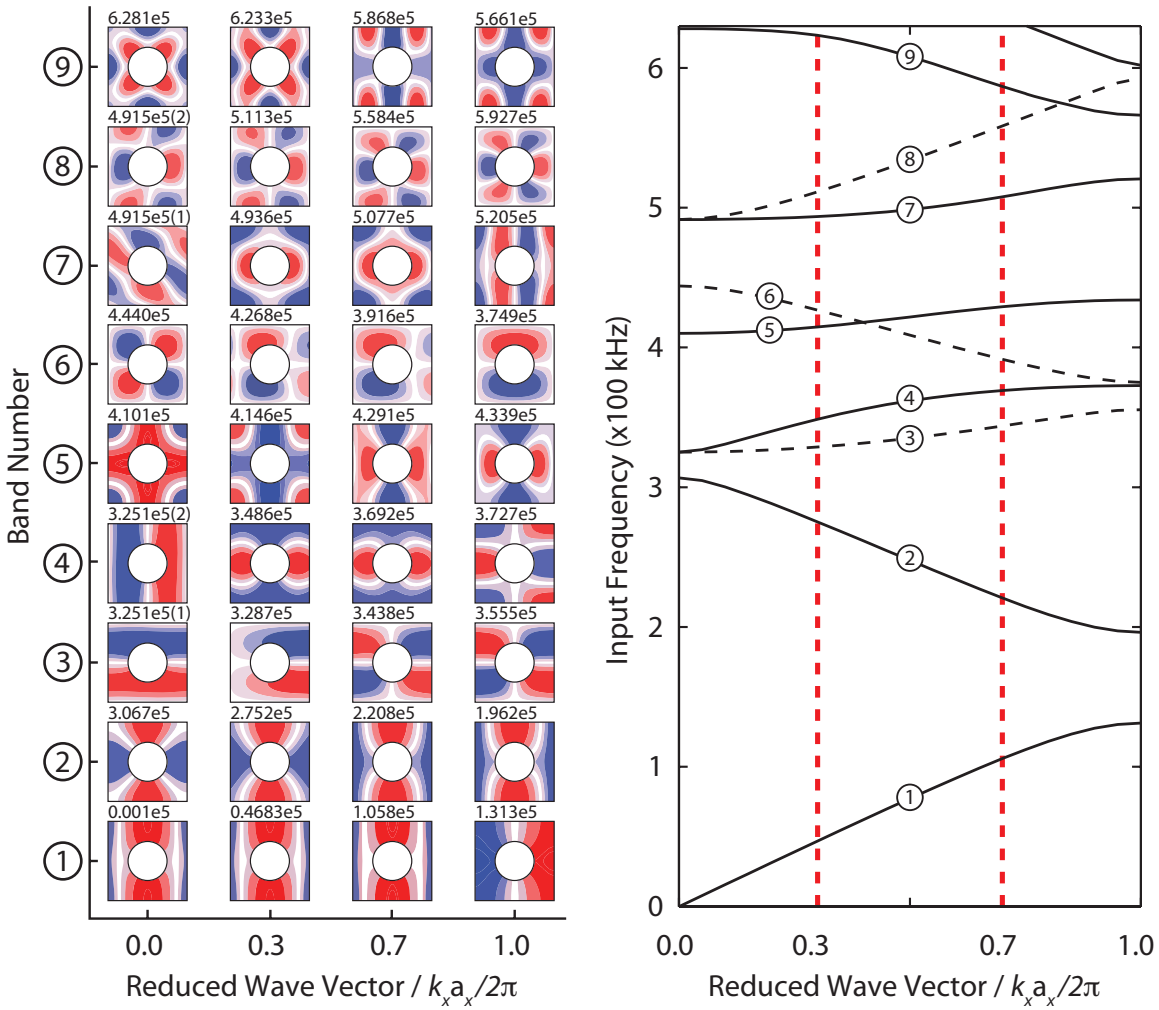


Figure 3.9: Complete pressure field mapping for the base case phononic crystal taken from computed band structures. (Left panel) Pressure mode shapes for the first nine dispersion bands at four specific reduced wave vector locations. (Right panel) Computed $\Gamma - X$ band structure of the base case phononic crystal showing the location of observed transmission gaps as well as the location of transverse modes (dashed curves).

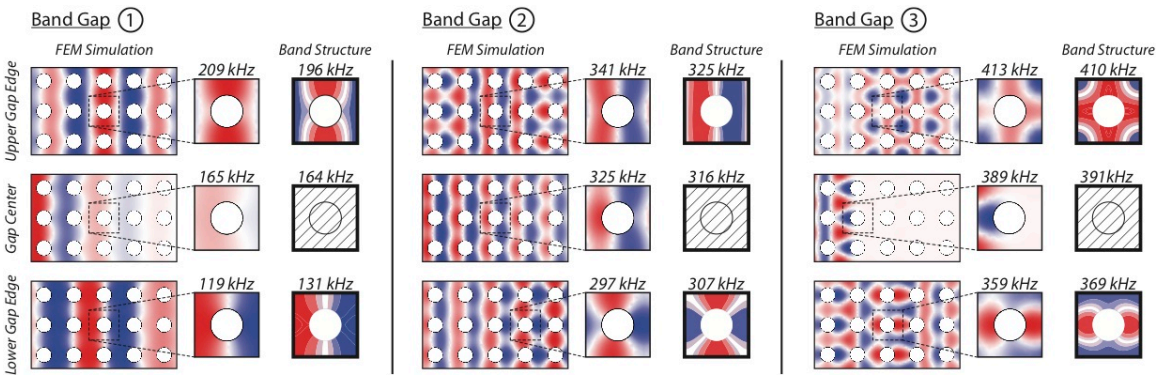


Figure 3.10: Pressure field validation at the gap edges using $n_x = 5$ data from Figure 3.8. For band gaps 1-3 (left, middle, and right, respectively): pressure field images reflect FEM Simulation and Band Structure results taken at their respective gap edges as well as the gap center (note: for band structure, no solution exists within the gap). Images reveal the presence of the infinite lattice modes, predicted from the band structure, in the FEM simulations.

scattering mechanics of the modes in question. Within the band gap, the pressure field decays as an exponential with increasing distance into the lattice — an observation that is consistent with the formation of a standing wave in the band gap. This decay is much more subtle in the case of the mass-loading gap owing to the small magnitude of the radiation impedance. However, in the infinite limit, this decay would be total. Decay is especially pronounced for the higher frequency gaps (Figure 3.10, right) as multiple scattering modes involve far more scattering centers than those from planar Bragg scattering thus producing standing waves of greater strength which, in turn, reject a larger fraction of the incident acoustic energy.

Our discussion thus far has been limited to longitudinal transmission, however, it is important to note that numerous applications demand that crystal transmission be tailored in multiple directions. In vibration control, for example, it is often desirable to want to block wave transmission in all directions simultaneously. For multidirectional transmission information, the band structure analysis just described can be extended to include all possible incident wave polarizations; providing a complete mapping of the band gaps of a given material. This is accomplished by parametrically sampling

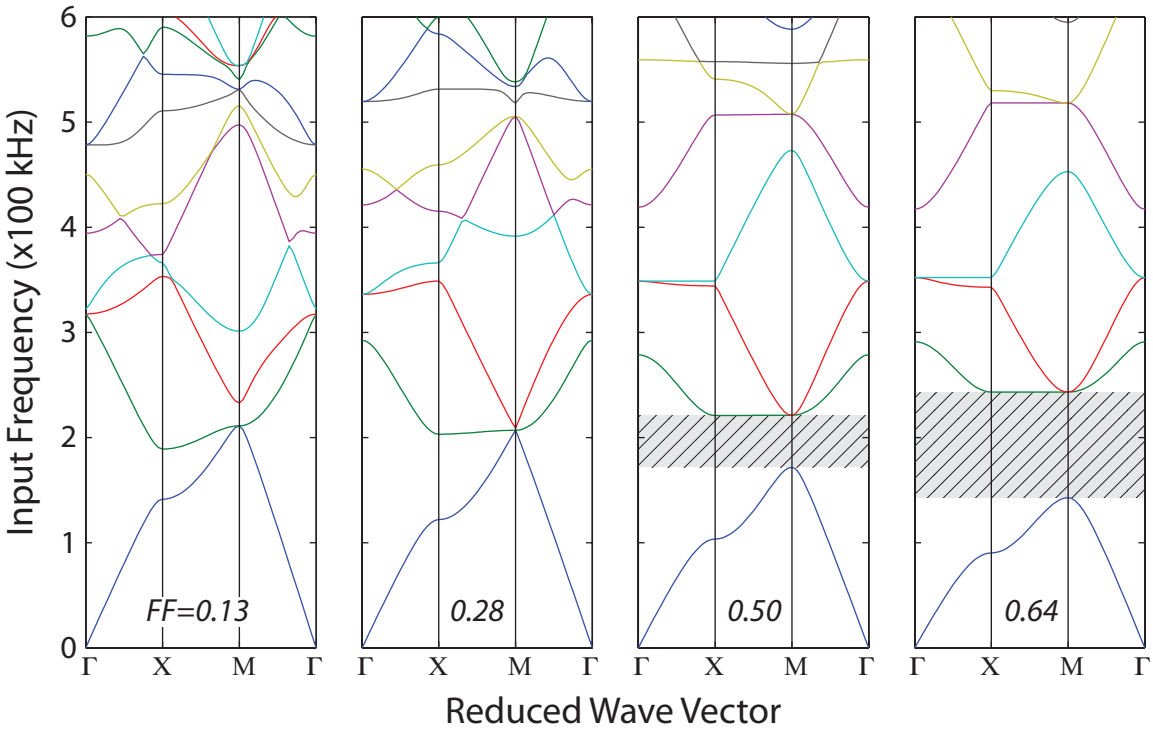


Figure 3.11: Complete band structure calculation of base lattice for various filling fractions (FF). (left to right) Full band structure of base case lattice along the three high symmetry directions of the first irreducible Brillouin zone ($\Gamma - X - M - \Gamma$) for FFs (obtained via isotropic scaling of inclusion radius, $r$) equal to 0.13, 0.28, 0.50, and 0.64. A total band gap is observed for filling fractions greater than 0.28. Within total gap region wave propagation is forbidden in all directions.

the entire periphery of the first irreducible Brillouin zone $\Gamma - X - M - \Gamma$. The profiles obtained for each leg of this trip, reflect the transmission properties along a specific high symmetry direction through the crystal. Consequently, band gaps that persist throughout the entire tour of the Brillouin zone represent areas in the frequency domain where wave transmission is theoretically forbidden in all directions. As an example, a complete gap is opened in the base case lattice by a slight increase in fill fraction, as shown in Figure 3.11. In Figure 3.11 we see that a complete band gap opens up for inclusion radii between 300 $\mu$m and 400 $\mu$m ($r/r_{\text{base}}$ between 1.2 and 1.6) corresponding to a filling fraction between 0.28-0.50. In-depth discussion of the conditions for forming total band gaps is the subject of future work.

## 3.4 Conclusion

Numerous geometric properties of 2D phononic crystals have been examined with regard to their associated influence on the emergence and evolution of band gaps. While two-dimensional phononic crystals have previously been studied, the treatment of lattice geometry has thus far been cursory. FEM simulations were used to generate transmission profiles for finite crystal arrays confined within theoretically infinite ducts. The results illustrate the richness of the influence of lattice geometry on the properties of transmission band gaps. A 1D TMM approach was employed as an intuitively tractable analytical model for approximating the transmission characteristics of the 2D crystals while also minimizing computational demands. It was found that transmission profiles of the 2D simulations were well reproduced by introduction of a set of effective waveguide dimensions. Profiles of the 2D crystals were compared with calculated band structure, *i.e.*, transmission in the infinite limit. Band structure results agreed remarkably well with the transmission characteristics of the duct-confined systems despite the finite scale of the simulated crystals.

# CHAPTER IV

# ADVANCES IN MODULAR MICROFLUIDIC CONSTRUCTION

## 4.1 Introduction

Microfluidics devices are particularly advantageous for biological analysis [25, 58–61] and high-throughput screening [62–64]. However, despite their financial and scientific benefits (*e.g.* experimental parallelization, reduced reagent consumption, short analysis times, portability, the ability to create bio-mimetic structures [65]), widespread adoption of such devices in the research community has yet to occur. One reason for this may be that a significant gap typically exists between the producers of microfluidic technologies (mainly engineers) and end users, the majority of which reside in the life sciences. The high cost and expertise often required to fabricate custom microfluidic devices [66], it would seem, remains a sufficient deterrent to those researchers who might otherwise benefit from the technology. As such, the development of technologies which enable custom microfluidic fabrication without demanding substantial investment and/or expertise will go a long way toward closing this gap.

Interestingly, the field of microfluidics is divided into two, essentially independent, branches of technology development. One branch is industrial, and is devoted to

the development of lab-on-a-chip technologies for the purposes of commercialization. Devices in this category typically focus on the transformation of multiple laboratory steps into unit operations contained on disposable/swappable micro-device. These devices then interface with a permanent master unit that handles fluidic actuation and data collection. The other branch, which is more relevant to this work, resides in academia and is primarily concerned with the development and use of microfluidics as either workhorse research tools or as custom devices for highly specific applications. Not surprisingly, many developers in this branch concerned with the utility rather than marketability of microfluidic devices and

A number of researchers have proposed simpler fabrication methods [11–14, 67] aimed at the elimination of costly and time consuming clean-room lithography. To replace the conventional chrome photomask, for example, Duffy *et al.* introduced the use of high-resolution transparencies [11]. Glennon *et al.* went further, moving to direct printing of the lithographic mold — laser toner, in this case, serving as the fluidic structures [12]. This approach is limiting however, as it only allows for a maximum channel height of $\approx$10 $\mu$m which is problematic for some biological applications [67]. Others went further still, creating more topologically diverse molds using solid object printers (SOP) [14]. But SOP is not ideal due to the substantial cost of the equipment an its generally limited resolution ($\approx$250 $\mu$m minimum feature size). A clever technique employing direct printing on shrinkable thermoplastics was recently proposed by Grimes *et al.* and is potentially useful for fabricating channels in the range of 50-100 $\mu$m [13].

Modular architectures utilizing fluidic breadboards and prefabricated microfluidic components are a popular development of late [16–18]. This approach, more than any other, is amenable to ubiquitous distribution among research scientists as prefabricated components would allow for standardization and point of use customization. However, the use of a breadboard places inherent limitations on the flexibility of

such systems. Recently, Rhee and Burns developed a modular microfluidic assembly block (MAB) platform [15] using pre-fabricated PDMS blocks. With this approach, non-expert users could assemble fully-customizable microfluidic devices within minutes at the point of use. Furthermore, this approach did not require the use of a complex breadboard interface.

Here we report on an advanced MAB concept employing PDMS blocks with assorted channel geometries that are linked together and bonded to form fully functional microfluidic devices (see Figure 4.1). Specifically, we introduce: (1) flexible ice-cube tray casting to replace rigid SU-8 molds, greatly increasing the speed and ease with which MABs can be fabricated and extracted, (2) the use of pre-coated substrates and the methodology for their preparation utilizing inexpensive "off-the-shelf" tools, and (3) a new block design featuring self-aligning structures as well as small radii on the sealing faces of the male MABs for improved sealing at block junctions. The combination of these advances allows rapid assembly of MABs into a variety of working devices.

## 4.2 Materials and Methods

### 4.2.1 SU-8 Master Mold Preparation

MAB fabrication begins with preparation of master mold structures in SU-8. These precursor SU-8 master molds were constructed in two steps using standard photolithography. First, a thin (50-100 $\mu$m) layer of fluidic structures comprised of assorted channel geometries was deposited. Second, thicker (250-1200 $\mu$m) structures which define the walls of the MABs were added. The fluidic layer of the mold was prepared by spin-casting either SU-8 2025 or SU-8 2035 (MicroChem Corp.) onto bare 4 inch silicon wafers (500 $\mu$m thick) to a desired feature height, typically 80 $\mu$m. Once coated, wafers were allowed to rest for 5 minutes before being transferred to a

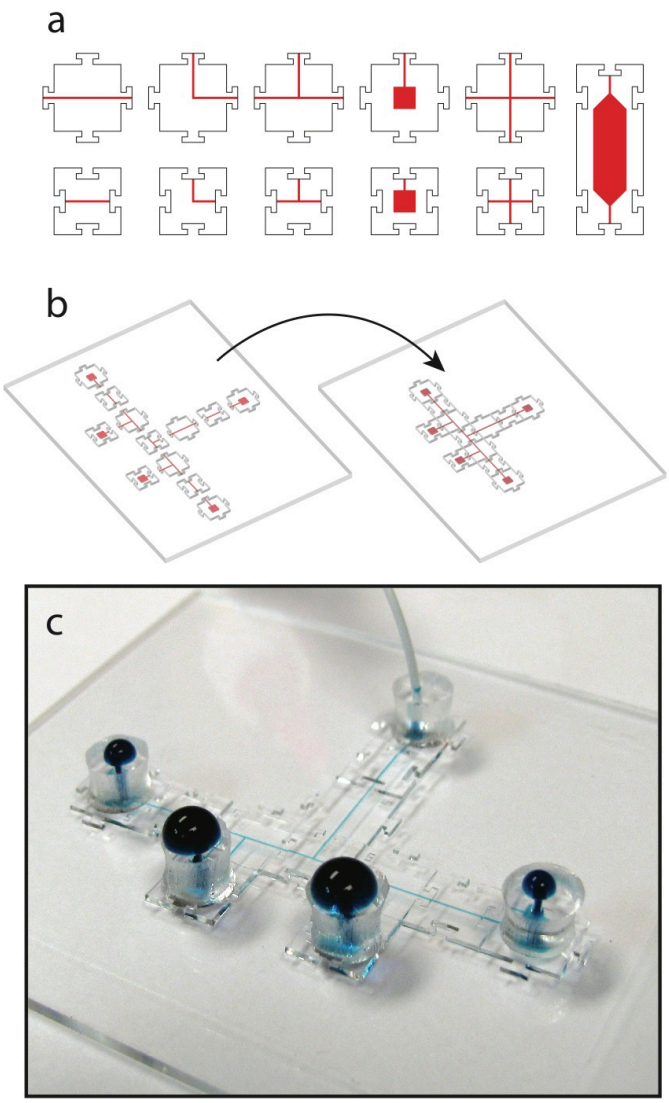


Figure 4.1: The MAB concept. (a) Schematic representation of the assorted male and female MABs used in this work (b) A selection of pre-fabricated MABs prior to (left) and following (right) assembly and bonding. (c) Photograph of actual MAB device, of identical construction, during a flow test.

level hotplate with a perforated cover and soft-baked for 5 minutes at 65 °C followed by 20 minutes at 95 °C, ramping the temperature slowly (2 °C/min) to ensure smooth solvent evolution. After cooling to room temperature, edge beads were removed by gentle application of a clean room swab soaked in EBR-PG (MicroChem Corp.) with wafers rotating at 500 RPM. De-beaded wafers were exposed on a contact aligner for ≈25 seconds (500-750 mJ/cm$^2$) against a chrome photomask containing the fluidic features (see Appendix A Figure A.1a) and allowed to rest for 30 minutes before undergoing a post-exposure bake at 65 °C for 3 minutes and 10 minutes at 95 °C, again gently ramping the temperature up and down on a hotplate with a perforated cover. Once cool, wafers were submersion developed in fresh SU-8 Developer (MicroChem Corp.), rinsed with IPA, and gently blown dry with compressed air or nitrogen.

Mold walls were prepared in a similar fashion, by spin-casting SU-8 2150 (MicroChem Corp.) directly on top of the fluidic structures just described. Spun films were covered and allowed to settle on a level surface for approximately 1 hour prior to soft baking. Trapped bubbles in the resist film that were not liberated during the rest period were coaxed out of the resist film by heating the wafers for approximately 30 minutes in a solvent-rich environment, *i.e.*, completely covered with a glass dish, to 65 °C. Any remaining bubbles were ruptured manually, replacing the glass dish as necessary to maintain a solvent-rich air/resist interface. Bubble-free resist films were subsequently soft-baked at 95 °C for approximately 7 hours, again ramping the temperature slowly (2 °C/min). Once cool, edge beads were carefully removed using the procedure described above. Following the soft-bake, wafers were aligned to a chrome photo-mask patterned with the assembly block walls (Appendix A Figure A.1b) and exposed. For example, an approximately 500 $\mu$m film was exposed for 90 seconds or 2300 mJ/cm$^2$. Wafers were then allowed to rest for 30 minutes prior to undergoing a low temperature post-exposure bake at 55 °C for 2 hours, during which time, a very slow temperature ramp (1 °C/min) is utilized in order to minimize internal stress in

the final SU-8 structures [68]. After returning to room temperature, the wafers were submersion developed for 20-30 minutes (depending on the film thickness), rinsed with IPA, DI water, then allowed to air dry. Molds were subsequently treated with $O_2$ plasma and placed in an evacuated vessel along with 20 $\mu$L of tridecafluoro-1,1,2,2-tetrahydrooctyl-1-trichlorosilane for 1 hour. A complete schematic representation of SU-8 master mold preparation is shown in Appendix A Figure A.2.

### 4.2.2 Mold Replication in Silicone

Durable and flexible silicone replicates of the SU-8 master molds were fabricated using a commercially available, low-viscosity liquid silicone rubber (CopyFlex - MYOM, Cincinnati, OH) with a working time of approximately 4 hours. Completed SU-8 master molds were placed in a casting tray and encapsulated with the two-component CopyFlex® liquid silicone, prepared according to the manufacturer's recommendations. To ensure an accurate and void-free mold impression, the encapsulated molds were subjected to 30 inch. vac. Mercury for 10-20 minutes. Subsequently, the molds were baked in the oven at approximately 80 °C for 2 hours. Once cool, a perfect positive (+) impression of the master mold is recovered by gently peeling away the cured silicone, which releases effortlessly as a result of the silane treatment discussed above. Failure to silanize the SU-8 precursor resulted in unwanted bonding and often destruction of the master mold. The negative (-) impression of the SU-8 structures was recovered by a repetition of the same silanization and encapsulation procedure just described ending with the silanization of the recovered negative.

### 4.2.3 Assembly Block Casting

Large populations of defect-free MABs were rapidly produced by casting ≈9:1 (base:catalyst, by weight) mixture of PDMS (Sylgard 184, Dow Corning) within the recessed wells of the final silanized silicone molds. The casting procedure was per-

formed by applying an amount of PDMS sufficient to cover the entire mold to a height just above the mold surface. The covered mold was then placed in 30 inch. vac. Mercury for ≈5 minutes or until a quiescent, bubble-free, PDMS film was observed. Then using a standard razor blade and applying a modest amount of pressure, excess PDMS was slowly drawn off the mold surface. The best results were achieved by sweeping the razor blade diagonally across the mold furrows with the blade angled slightly in the direction of travel (≈30-45 °). Due to slight compression of the silicone surface during this procedure (necessary to minimize residual PDMS at the top of the mold walls), it was often necessary to backfill some of the wells. These wells were easily identifiable in good light due to their concave liquid surfaces. Backfilling of wells was accomplished by loading ≈200 $\mu$L of PDMS into a 1000 $\mu$L micropipette tip, removing the tip from the micropipette and using the semi-filled tip as a capillary restrained liquid hopper. Once filled, mold was placed in the oven for approximately 1-2 hours at 80 °C. Cured MABs were then readily removed by flexure of the mold and extraction with dull tweezers. Using this procedure, virtually every usable MAB (wells at the periphery of the mold are often useless as a result of the edge bead removal) was routinely extracted without damage to either the mold or blocks in a matter of minutes.

### 4.2.4 Substrate Preparation

To prepare a given substrate, a liberal amount of PDMS (1:1) was dispensed onto the glass surface. Then, this liquid was spread into a think film by slowly walking a jet of compressed air or nitrogen in a steady zigzagging pattern over the entire length of the substrate with the jet situated at roughly a 30-45° angle relative to the substrate surface. The jet was formed using a simple compressed air gun with on/off toggle fitted with a 2 mm ID nozzle (≈ 1 cm in length) in conjunction with a course upstream pressure regulator and gauge. This procedure was repeated until

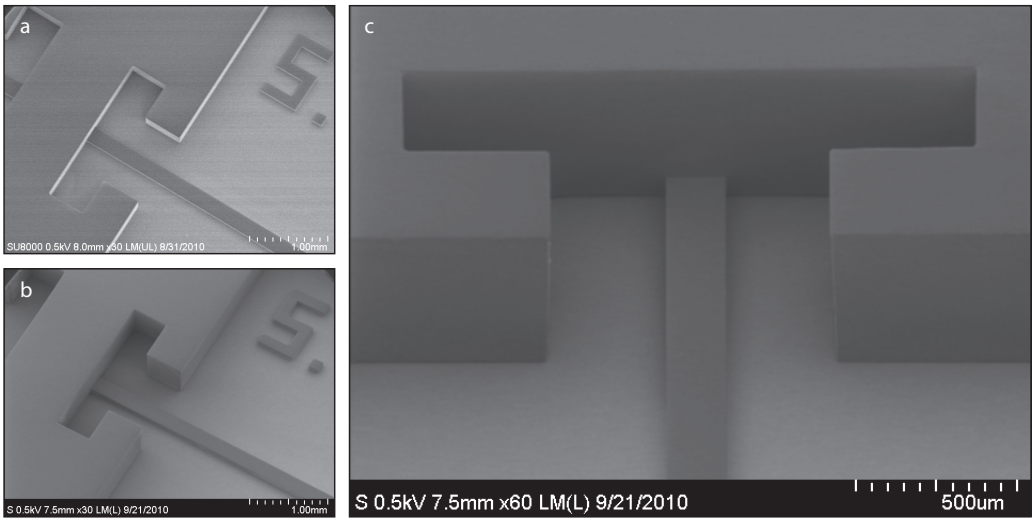


Figure 4.2: SEM images of precursor SU-8 master molds. (a) Mold with ≈250 $\mu$m thick walls and 80 x 200 $\mu$m fluidic channels. (b) Mold with ≈500 $\mu$m thick walls and 80 x 200 $\mu$m fluidic channels. (c) Image of mold in (b) illustrating the negative pitch or sidewall irregularity that was typically observed

an advancing liquid front was no longer visible on the substrate surface. For a 2 x 1 inch glass slide, this took approximately 1 minutes. After the thin-film was spread, substrates were then allowed to rest for 5-10 minutes prior to MAB assembly.

### 4.2.5 Device Assembly

Devices were assembled in a stepwise fashion, on pre-coated glass substrates, by linking the MABs necessary to realize a given design using a pair of fine point tweezers. Scotch tape (3M Corp) was used to remove dust and particulates from the channel side of the MABs prior to use and a standard stereoscope was used, though was not required, as a visual aid during the assembly process. Linking of blocks was greatly facilitated by placing the MABs, insofar as possible, directly in their desired location. A preferred approach was to lean the connecting end of the MAB on the relevant block then depress the alignment keys until the channel side of the block made contact with the liquid film. Once seated, it was typically necessary to press on the block surface to liberate any air bubbles that may have become trapped. This process

was repeated, periodically checking the overall alignment, until the target design was realized. Following assembly, completed devices were transferred to a 140 °C hotplate to cure for ≈ 5 minutes. Once cooled, PDMS posts for fluidic interfacing were affixed to inlet/outlet MABs using a straightforward stamp and cure approach or, optionally, $O_2$ plasma bonding. Leaks, if present, were quickly repaired by simply returning the device to the 140 °C hotplate and applying a very small amount of PDMS (1:1) to the effected junctions. For high pressure applications or if a more robust device was desired, bonded MAB assemblies were fully encapsulated in a thick layer of PDMS (10:1).

## 4.3 Results and Discussion

### 4.3.1 SU-8 Fabrication

SU-8 master molds were constructed using a multi-step photolithographic approach. Completed molds consisted of thin fluidic structures (typically 80 $\mu$m), with a variety of channel designs, and thick walls (typically 250-500 $\mu$m) that defined the periphery of the MABs. Adjustment of channel and wall dimensions were possible by alteration of spin speed, use of alternate SU-8 formulations, or by the successive addition of multiple spin and bake cycles [15]. SEM images of two completed master molds are shown in Figures 4.2a and 4.2b. Final SU-8 structures possessed very smooth sidewalls with sharply defined boundaries — two features critical to the quality of inter-block alignment and sealing. A slightly negative or overhanging pitch to the SU-8 sidewalls (Figure 4.2c) was typically observed regardless of the mold wall thickness. This phenomenon results from the use of a broadband UV source on the contact aligner and could be eliminated by installation of a long-pass filter to block UV transmission below 350 nm. Sidewall overhang manifests itself, in this case, as V-shaped crevices between adjacent MABs. The consequence of this, depending

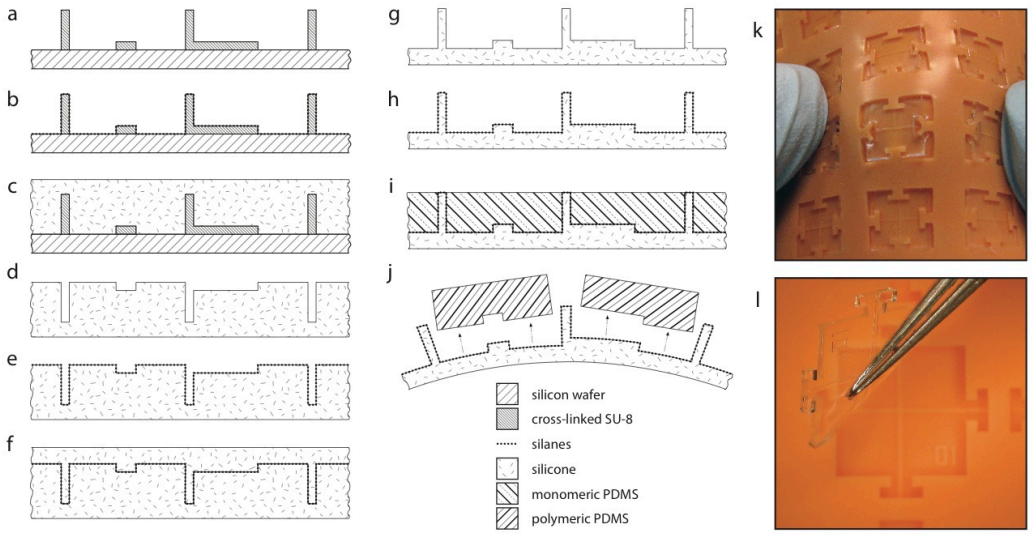


Figure 4.3: Schematic representation of replication of SU-8 master molds in flexible silicone. (a) Pre-cursor master mold constructed from SU-8 on a 4" Silicon wafer. (b) Chemical surface modification of *(a)* with trichlorosilanes. (c) Encapsulation of *(b)* with liquid silicone. (d) Positive silicone cast following release. (e) Chemical surface modification of *(d)* with trichlorosilanes. (f) Encapsulation of *(e)* with liquid silicone. (g) Recovery of negative silicone cast following release. (h) Chemical surface modification of *(g)* with trichlorosilanes. (i) Filling of MAB wells with PDMS monomer. (j) Following PDMS polymerization, MAB's are released by flexure of the silicone mold. (k) Image of actual 250 $\mu$m silicone mold during step *(j)*. (i) Extraction of a male MAB using a pair of blunt tweezers.

upon the severity of the overhang, are inter-block gaps that potentially extend to the channel floor.

It is worth noting that thick SU-8 processing was made particularly difficult by the development of high internal stresses in the final cross-linked epoxy. For SU-8 structures thicker than $\approx$250 $\mu$m, it was common to experience — even with careful preparation — severe cracking, de-lamination, substrate deformation, and resist distortion. These issues were all but eliminated after implementing a protocol similar to one developed by Li *et al.* who used extended soft-bake times, lower post-exposure bake temperatures, and slow temperature ramping, in order to achieve final SU-8 structures with 70% less internal stress and 50% greater tensile strength [68].

### 4.3.2 Flexible Casting Trays

MAB extraction from rigid SU-8 master structures requires the delicate use of sharp tools such as syringe needles or razor blades [15]; however, even with great care, it is difficult to avoid gouging the sidewalls of the SU-8 and/or damaging the MABs themselves in the process. To address this, we developed a casting approach which facilitates MAB extraction while also preserving the integrity SU-8 masters. The approach, illustrated in Figures 4.3a-4.3j, utilizes a low-viscosity liquid silicone rubber to create near-perfect — some benign surface roughening was observed (see Appendix A Figure A.3) — replicates of the original SU-8 master structures. Silicone rubber replicates are highly flexible and durable, allowing for the production of MABs with greater rapidity and ease without causing damage to costly SU-8 master structures. Chemical treatment of the silicone replicates with trichlorosilanes was found to yeild a passivated surface that did not bind to PDMS. MAB extraction, as such, was trivially performed by flexing the casting tray and extracting the MABs with a pair of dull tweezers (see Figure 4.3k and 4.3l). With this process, it was common to harvest an entire tray's worth of MABs (50 - 60 blocks) with nearly 100% success in only minutes, and hundreds of MABs within a few hours. An additional benefit to this approach is that affords other opportunities for potential end users, namely, the option to make one's own supply of MABs.

Some thickness variation among extracted MABs was observed. These variations ($> 100$ $\mu$m in some cases) arose from insufficiently leveled hot plates during the soft-bake and post exposure bake steps of the lithography. Female MABs were found to be thicker, on average, than males regardless of master mold thickness ( see Appendix A Figure A.4). This difference in overall piece thickness reflects the consistent orientation with which the wafers were placed in the hotplates. Note that these variations did not appear to effect the performance of planar MAB assemblies. However, such variations would inhibit realization of three-dimensional, multi-layer, MAB devices.

Development of multi-layer MAB structures is the subject of ongoing work and will allow for more advanced microfluidic components such as peristaltic pumps, valves, and fluidic logic structures [69, 70] to be created in the same manner as a planar MAB device.

### 4.3.3 Block Design

Abrupt deviations in channel cross-section and/or flow direction can pose problems for microfluidic systems by introducing sharp pressure drops and small pockets of stagnation in the flow. Thus, the fabrication method used should yield devices with reliable hydraulic diameters. Toward this end, MABs were modified to include jigsaw-like lock and key (male and female) structures (Figure 4.4a). These structures fix the relative orientations of neighboring MABs thus ensuring both local and long range alignment of the fluidic network. The sealing face of the male MABs were also modified to include very small trapezoidal extensions (henceforth referred to as the piece *convexity*) of 0, 2, 5, and 10 $\mu$m (see $\delta$, in Figure 4.4a). Alignment and offset data for numerous MAB junctions at each convexity is shown in Figure 4.4b. Detailed statistics of channel offset and alignment angle are plotted in Figures 4.4c-4.4f. The interquartile range of the relative channel offset ($\alpha/w$), for example, was found to be $\pm 0.06$ with a maximum recorded offset of $\approx 0.2$. Similarly, the relative channel angle ($\theta - 180\,^\circ$) was found to be approximately $\pm 1.0\,^\circ$ with a maximum angle deviation of 3.0-4.0 $^\circ$. Note that channel offset and angle do not appear to be a function of piece convexity; however, the data for 0 $\mu$m convexity displays the tightest range in each case.

Elimination of inter-block gaps is important to the functionality of completed MAB devices. To minimize the occurrence of inter-block gaps (mathematically defined as the distance between two blocks at the channel roof) varying amounts of convexity were added to the sealing face of the male pieces. By incorporation of this

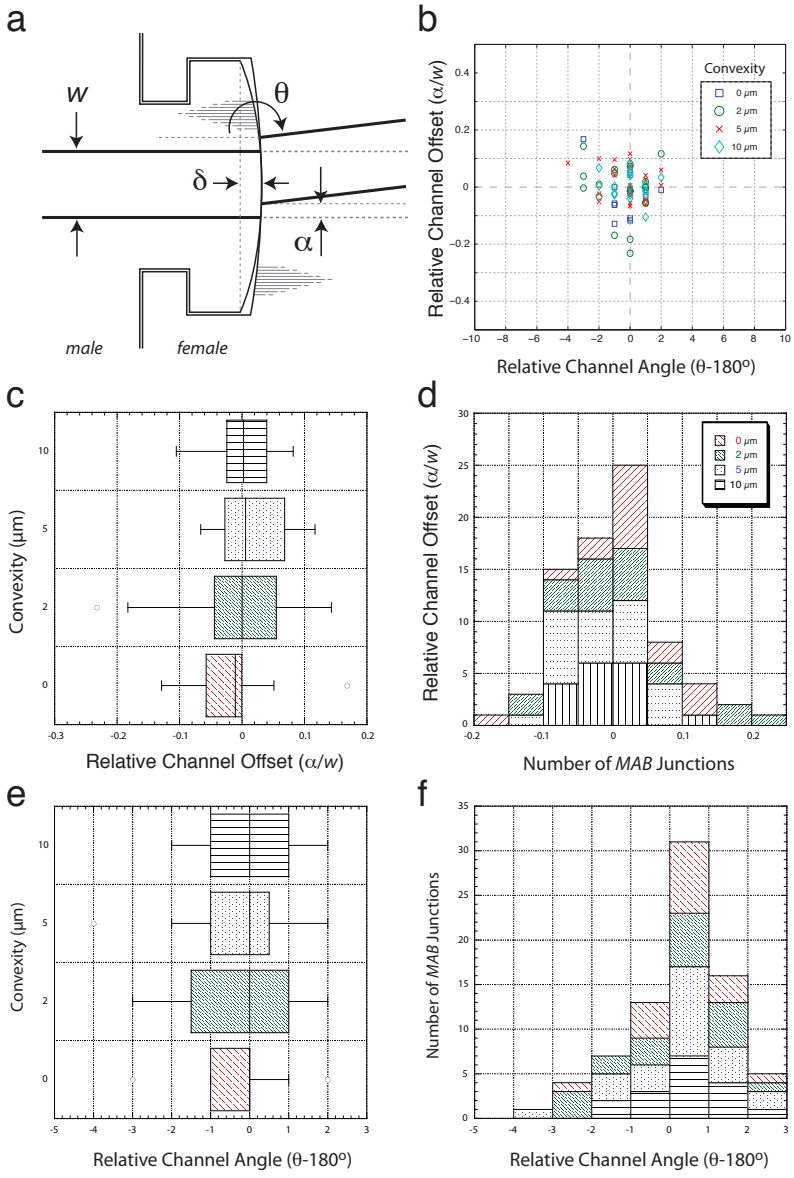


Figure 4.4: Channel alignment and offset statistics for a random sampling of MAB junctions with various piece convexities. (a) Schematic illustration of a MAB junction highlighting relevant parameters: channel width (w), channel offset ($\alpha$), channel angle ($\theta$), piece convexity ($\delta$). (b) Bulls-eye plot of relative channel offset ($\alpha/w$) and relative channel angle ($\theta - 180°$) for $\geq 20$ MABs at each convexity. (c) Box plot of relative channel offset versus piece convexity. (d) Histogram of *(c)*. (e) Box plot of relative channel angle versus piece convexity. (f) Histogram of *(e)*.

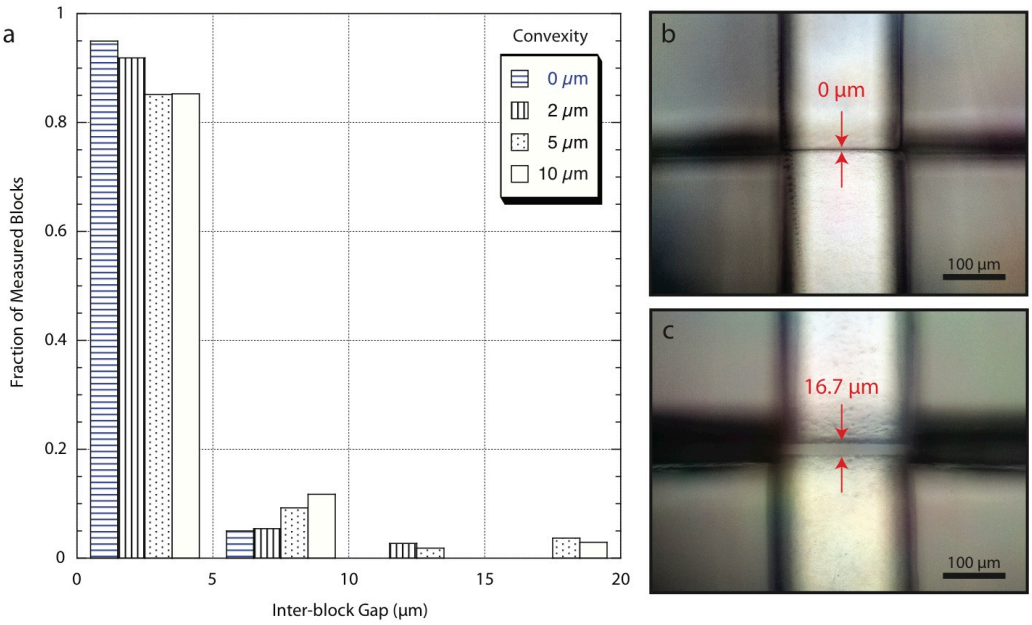


Figure 4.5: Inter-block gaps for a sampling ($N \geq 20$ in each case) of bonded MABs with different piece convexity. (a) Histogram of inter-block gap magnitudes for assembled and bonded MABs of various convexity (four bins: 0-5 $\mu$m, 5-10 $\mu$m, 10-15 $\mu$m, and 15-20 $\mu$m). (b) Microscope image of a 0 $\mu$m gap. (c) Microscope image of a 16.7 $\mu$m gap.

additional material, it was thought that the sealing faces of two linked MABs would be held in a state of increased compression, thus decreasing the likelihood of gaps forming. Moreover it was thought that the presence of these minuscule PDMS cushions would compensate for the V-shaped crevices resulting from the negatively sloping sidewalls in the master structures mentioned above. Strangely, a sampling of bonded MAB junctions at each convexity indicates that an increase in convexity results in an increase in both the frequency and the magnitude of the observed inter-block gaps (Figure 4.5a). Despite this somewhat counterintuitive result, the vast majority of sampled junctions ($> 80\%$, regardless of convexity) exhibit inter-block gaps of $\leq 5$ $\mu$m; moreover, within that group, the fraction of junctions displaying no gaps were 80%, 60%, 56%, and 56% for convexities of 0, 2, 5, and 10 $\mu$m, respectively. For illustrative purposes, a pair of such junctions with 0 $\mu$m and 16.7 $\mu$m gaps are shown in Figure 4.5b and 4.5c, respectively.

### 4.3.4 Substrate Preparation

Researchers often take advantage of the native stiction of PDMS in the design and construction of microfluidic systems. Stiction is problematic, however, when attempting to precisely position arrays of objects in close proximity to one another. For MABs, such a scenario is particularly undesirable because poor positioning of the blocks leads to non-functional devices. As such, we developed a simple means of preparing glass substrates for MAB assembly by coating them with thin-films of PDMS monomer. Our thin-films, the thickness of which is tunable over a range of 1-3 $\mu$m, serve as a lubricating layer upon which MABs can freely glide, allowing linked assemblies of MABs to settle into tight low-stress configurations. The thin liquid films have the added benefit of wicking up into the interstitial spaces between blocks allowing for covalent lateral linkage of the MABs during the heat cure step.

Preliminary determination of the optimal film thickness was accomplished by performing MAB assembly on a series of spin-coated (1:1) films with thicknesses of 2-22 $\mu$m. Note that the MABs used possessed channel depths of 60-80 $\mu$m. A film of $\approx$2 $\mu$m (6,000 RPM, 30 seconds) was found to be of sufficient liquidity to allow facile manipulation of the MABs and capillary wicking of PDMS into the block gaps, but was thin enough so that the fluidic channels did not readily flood during a routine assembly. However, because the purchase of a spin-coater is likely not feasible for most end users, numerous "off-the-shelf" methods were explored in an effort to reproduce the characteristics of the 6,000 RPM spun films. The average thickness and deviation for films prepared by: spin coater at 6,000 RPM, 40 psi compressed air, hand application with a clean room wipe, a razor blade drawn over bare glass, and a razor blade drawn over various etched glass recesses is plotted in Figure 4.6a. Of these methods, the use of a compressed gas jet was found to be superior, yielding films with a thickness and deviation comparable to those of the spin-coated benchmark films. Etched glass recesses, though ultimately effective in producing the target film thickness suffered

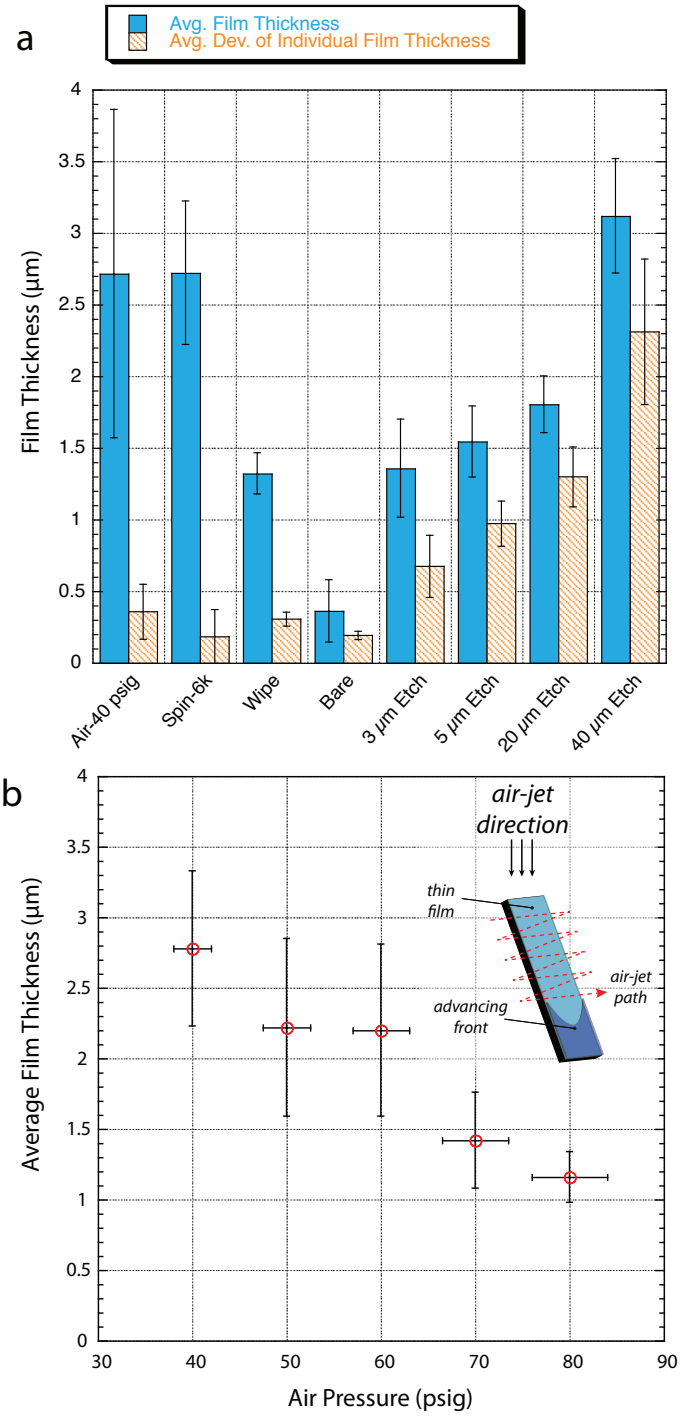


Figure 4.6: Summary of "off-the-shelf" methods for the preparation of PDMS thin-films. (a) Resulting average film thickness and variation for assorted preparation methods. (b) Film thickness calibration plot for preparation using a compressed air jet (see *inset*).

from poor uniformity, most likely due to the unavoidable deflection of the razor blade, and required the use of hazardous chemical etchants.

The compressed gas approach was further refined by addition of coarse pressure regulator allowing for controllable film thickness in the range of 1-3 $\mu$m. Figure 4.6b shows the resulting film thickness and associated standard error for substrates prepared by walking a compressed air jet in a zigzagging pattern (*inset*, Figure 4.6b) with gas pressures over the range of 40-80 psi. Ideal results for the MAB dimensions utilized here were achieved with an upstream gas pressure of ≈60 psi (measured under fully open flow conditions). It is worth noting that some minor variation along the substrate length, specifically a slight increase in thickness toward the substrate edge, was observed (Appendix A Figure A.5) using this technique. It is also worth noting that the optimal thin-film thickness should be catered to the channel dimensions of the MABs being used. MABs with fluidic features on the order of a few microns, for example, might require a thin-film prepared by drawing a razor blade over bare glass.

### 4.3.5 Assembly and Bonding

Condensation of the assembly and bonding steps of the MAB process greatly simplifies device construction. During assembly, the blocks float on a lubricating thin-film of PDMS monomer, enabling facile linkage, and allowing the blocks to settle into close, low-stress contact. Simultaneously, the PDMS film acts as a liquid reservoir, filling the interstitial gaps between MABs by capillary action (*inset*, Figure 4.7a). The ≈80 $\mu$m MAB channels used in this work were sufficiently large compared to the PDMS film thickness so as to provide some leeway when sliding or reorienting a device during assembly. It is worth noting, however, that excessive sliding did result in a flooded channel. When this happened the affected MAB(s) were simply removed and replaced with fresh blocks. Capillary re-distribution of the thin liquid film was not observed to be a problem in such cases.

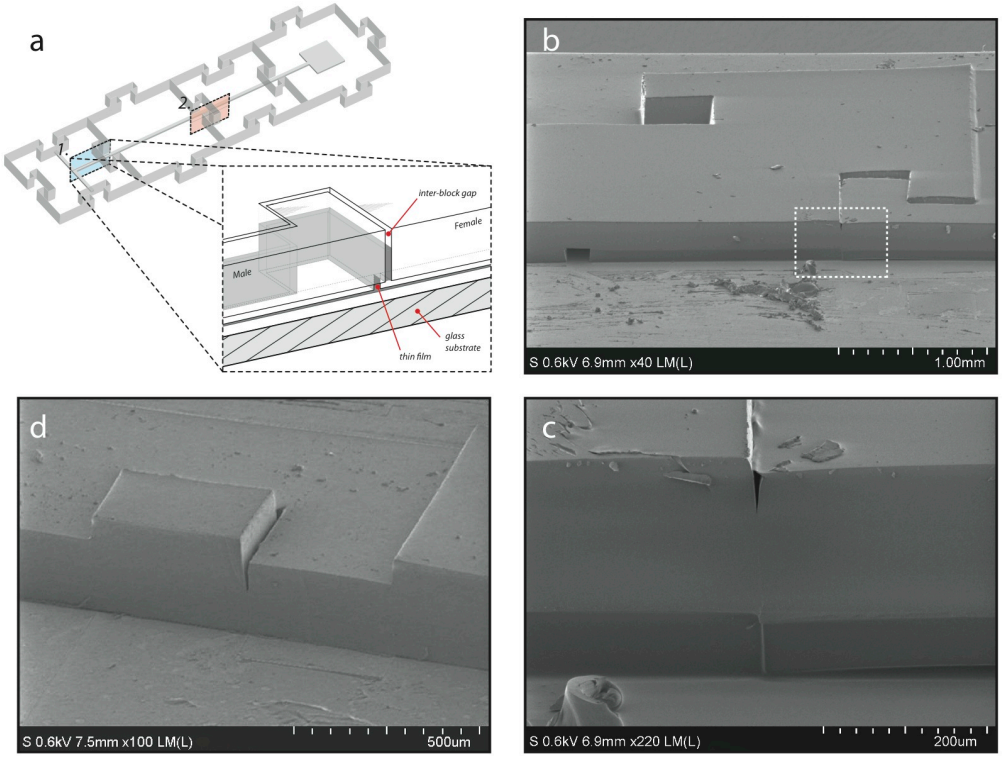


Figure 4.7: (a) Schematic illustration of an assembled MAB device and detail (*inset*) of the device cross-section shown by plane No. 1 highlighting the capillary wicking of the liquid film into the inter-block gap. (b) Companion SEM image of the cross-section defined by plane No. 1 in an actual MAB device with the same channel geometry. (c) Close-up of the highlighted rectangle in *(b)* showing the bond which has formed at the MAB junction well above the channel roof. (d) Companion SEM of plane No. 2 in *(a)* showing the vertical bond penetration extending from the substrate surface $\approx$150 $\mu$m.

Lateral and surface bonding of MAB assemblages occurs in minutes after placement on a 140 °C hotplate. Figures 4.7b-4.7d show SEM cross-sections of some example MAB devices following the bonding step. Notice that the block interfaces have formed a continuum due to the capillary penetration of the PDMS liquid film. When necessary for high-pressure applications ($> 5$ psi) or simply when a more robust device was desired, finished MAB devices were encapsulated in a thick ($\approx$0.5 - 1 cm) layer of PDMS. The result is a finished device that is virtually indistinguishable to one produced using conventional soft lithography.

Leaks were occasionally observed during fluidic testing of finished MAB devices owing to the presence of inter-block gaps, but were easy to fix. When present, leaks were invariably found to occur at inter-block junctions and always vertically upward through the V-shaped crevice between pieces. It is important to note that in such cases the utility of the device was rarely lost. In fact, the repair of leaks was found to be quick and straightforward. Such a device was simply returned to the 140 °C hotplate and a small amount of PDMS (1:1) was applied on the effected junctions using a loaded micropipette tip. The polymerization time, given the small amount of PDMS and the high catalyst ratio, was on the order of a few seconds. Thus, even relatively large inter-block gaps ($\approx$20 $\mu$m) were routinely repairable as the PDMS, which rapidly fills the inter-block region, polymerizes before any channel flooding could occur.

## 4.4 Exemplary Applications of MAB Devices

### 4.4.1 Chemical Gradient Synthesis

Fine spatial control of chemical gradients is helpful the study of cellular populations, where it is often desirable to probe for toxicity limits over a wide range of concentrations. Using a traditional experimental approach, this would require prepa-

ration of a series of dilutions and simultaneous monitoring of a number of experiments in parallel. The same task is made far simpler in a microfluidic system with the aid of a chemical gradient generator. Such a device produces a spatial concentration gradient spanning the transverse dimension of a given micro-channel and can be finely tuned by adjusting inlet flow ratios. Using this approach, a continuum of toxicity data could conceivably be obtained in a single compact experiment.

The layout for a two-component version of such a device constructed from 58 MABs is shown in Figure 4.8a. The finished device, which has been encapsulated in PDMS for durability, along with gradient data generated by the device across the path M-M are shown in Figures 4.8b and 4.8c, respectively. Note the long-range alignment of the fluidic channels and the smooth nearly linear variation in the generated gradient.

### 4.4.2 Droplet Generation

Among its many documented applications, microfluidic droplet generation is very attractive as a means of culturing microbial consortia, where symbiotic nutrient exchange between constituent members is poorly understood. In a microfluidic setting, thousands of uniformly sized droplets containing a probabilistic distribution of unknown species can easily be generated in seconds. The sequestered droplets could then be incubated and later screened for symbiotic interactions. This form of high throughput screening requires narrow tolerances on the sizes of generated droplets as well as stability of the resulting emulsion.

Construction of such droplet devices is straightforward with MABs. Figure 4.8d shows an example of a simple flow-focusing droplet generator consisting of 12 standard MABs and 1 custom droplet collection/cultivation block. Images of the working device, after additional PDMS encapsulation to reenforce the large thin diaphragm of the droplet chamber, is shown in Figures 4.8e and 4.8f. A specialty surfactant

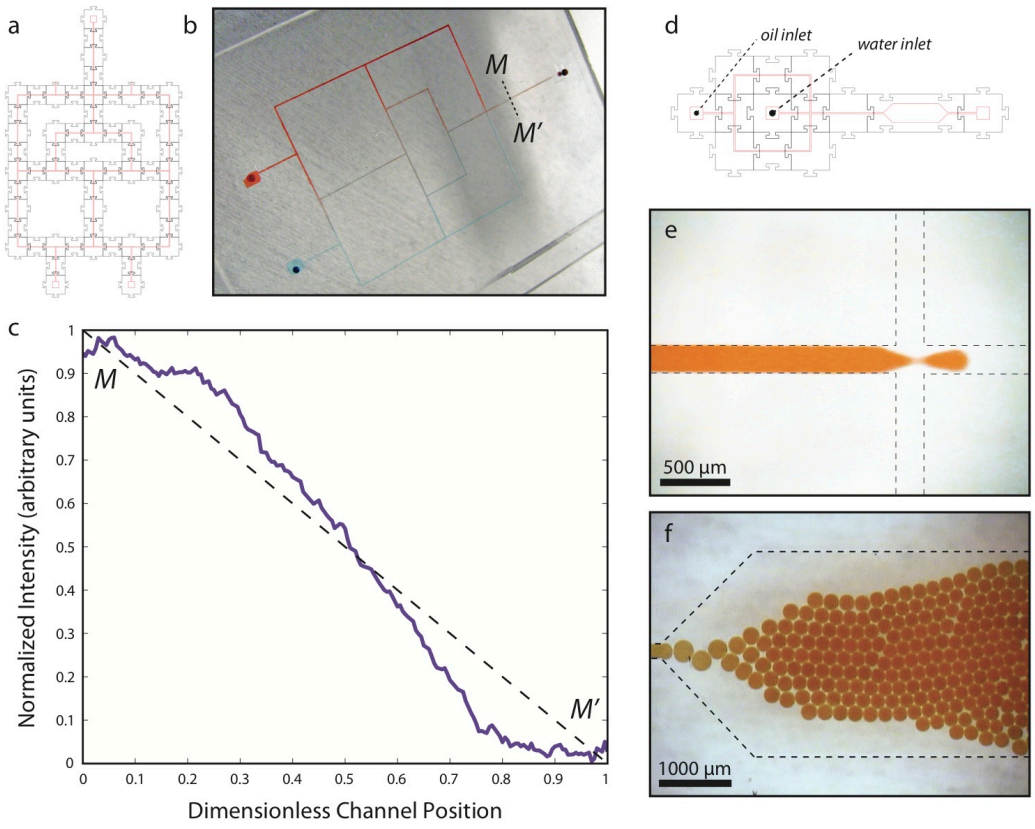


Figure 4.8: Chemical gradient and droplet generation in MAB devices. (a) Schematic of two component chemical gradient generator constructed from 58 MABs. (b) Image of completed MAB device following additional encapsulation in PDMS. (c) Pixel intensity plot illustrating the sigmoidal variation of the generated gradient along the path M-M' in *(b)*. (d) Schematic of 13 block flow-focus droplet device. (e) Close-up image of the device in *(d)* during operation illustrating the formation of a water droplet at the flow-focused junction (dotted lines are to illustrate channel boundaries). (f) Close-up image of the device in *(d)* during operation showing the generation and accumulation of highly stabilized and uniform droplets in the downstream chamber (dotted lines are to illustrate channel boundaries).

(RainDance Technologies, Inc.) was used to stabilize the generated droplets which can be packed into the droplet chamber and incubated for greater than 24 hours without coalescence — a necessary characteristic for in-vitro cultivation.

### 4.4.3 Total Internal Reflectance Microscopy

Total internal reflectance microscopy (TIR) is an indispensable experimental technique for studying the dynamics of single fluorophores. For single molecule researchers, particularly in the biological sciences, the most common method for imaging and probing their samples is to simply add them between a microscope slide and cover glass. Custom micro-channels are often created between these pieces using, for example, double-sided tape, wax, or Parafilm®. Later, holes can be drilled with diamond drill bits to allow for fluidic delivery of reagents and buffers. MABs offer a far more precise and straightforward means of fabricating these custom micro-channels as blocks with user defined dimensions are very easily assembled at the point-of-use and afford users options for flow and sample manipulation not possible with the conventional approach.

To demonstrate the use of MABs for both objective (Figure 4.9a) and prism-based total internal reflection (TIR) microscopy of small fluorescent nano spheres and single molecular fluorophores at or near the PDMS/water interface, single channel MAB devices were constructed on microscope cover glass (Figure 4.9b). During TIR excitation most microspheres (200 nm in diameter, suspended in a dilute water solution) were found to be in a state of brownian motion; however, many of the beads were found adsorbed to the $\approx$2 $\mu$m layer of PDMS at the glass boundary. TIR was readily apparent by comparing emission of intensely bright — due to their proximity to the evanescent TIR field — surface-bound beads with those of the freely diffusing beads (see Figure 4.9c). Adjusting the TIR to allow for epi-illumination of the buffer solution resulted in the beads in solution becoming readily apparent, and the diffusing

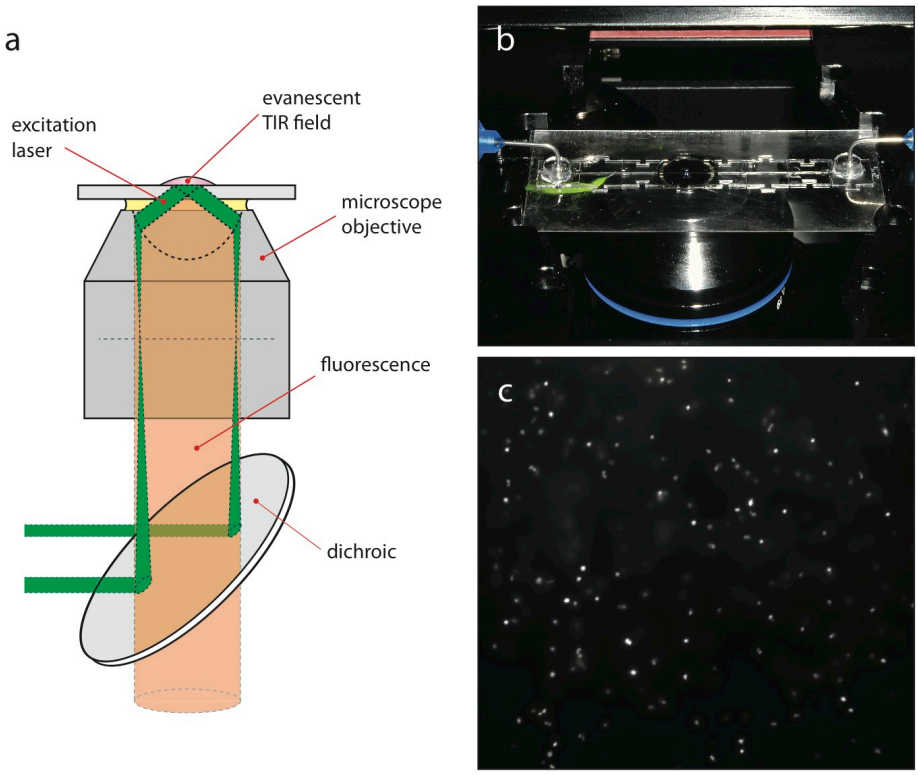


Figure 4.9: TIR Microscopy using MAB devices. (a) Simplified schematic of objective-based TIR microscope operation. (b) Image of 7 block straight channel MAB device, with attached fluidic inputs, on the TIR microscope stage. (c) Image from objective-TIR excitation experiment illustrating the contrast in signal strength for surface bound (bright) versus freely diffusing (dim) 200 nm nanospheres.

bead paths could be seen for long paths of travel as long as they were near the focus of the microscope. TIR was also verified by measuring the emission from the surface beads as the TIR angle was adjusted through a series of angles. The results show excellent promise for the use of MABs in many applications where imaging at the PDMS/buffer interface is needed. Similar experiments for prism-based TIR were also performed (data not shown).

## 4.5 Conclusions

The MAB approach presented is a simple and inexpensive alternative to traditional microfabrication techniques and is aimed at closing the gap between the developers of microfluidic technologies and the core potential user base in the life sciences. Anyone, regardless of discipline, can quickly assemble these building blocks into sophisticated microfluidic devices according to their own designs. In this work we discussed several advancements to the original MAB concept [15] including: the use of flexible molds for improved casting and extraction of MABs, the modification of the block design to include auto-alignment structures, analysis of the effectiveness of added material to the male structures for improved sealing, and the use of pre-coated substrates for condensing the assembly and bonding steps of the process. Exemplary MAB devices were also presented to illustrate that the technology could be readily applied to a variety of scientific applications. The MAB platform has no intrinsic limitations on the channel layouts or block dimensions used. Future users of MABs could work with fabrication foundries to develop custom sets of blocks to suit their specific needs. Simplified MAB production using flexible silicone molds affords users the additional option of producing their own supply of MABs. Optimization of precursor mold lithography will allow for MABs with highly uniform thickness and perfectly vertical sidewalls. Perfectly vertical sidewalls could eliminate inter-block gaps, and by extension, the need to repair leaks. Such improvements would enable the construction of multi-layer MAB devices with more advanced structures such as pneumatic control and fluidic logic.

# CHAPTER V

# CONCLUSIONS AND CONTINUING WORK

## 5.1 Conclusions

The overall aim of this dissertation work was to identify and develop new technologies for improving the usability of microfluidic tools, with specific emphases on micro-scale flow control and device fabrication. Our investigation of micro-scale flow control led us to develop a novel acoustic-based parallel pressure regulation scheme which was used to coordinate fluid motion within branched channel networks. In this scheme, an input acoustic signal consisting of one or more embedded frequencies were converted into a set of independently addressable output pressures via a unique coupling of resonance cavities and fluidic rectification structures. The device we constructed possessed four resonance cavities, each of which were tunable on the range of 0 - 200 Pa with a control resolution of $\approx$ 10 Pa. Using this system, we showed that versatile programmable fluidic manipulation was possible by interfacing the device with either droplet-based or continuous flow microfluidic systems.

Toward alternative acoustic flow control mechanisms, we conducted a detailed study of 2D phononic crystal microstructures focusing on transmission band gap properties related to perturbations in crystal geometry. Our results illustrated the richness of lattice geometry on the properties of phononic stop bands. In searching for computationally leaner alternatives to full FEM simulations, we found that 1D

waveguides possessing effective dimensions could very accurately reproduce 2D FEM transmission below, and in the vicinity of, the principle band gap. Finally, we showed that great insight into the transmission behavior of finite crystals could be gleaned by analysis in the theoretical infinitely spanning limit.

In order to make microfluidic prototyping more universally accessible to non-experts, we developed an advanced MAB methodology greatly reducing the time, cost, and expertise required for microfluidic device construction. We found that MAB casting and extraction were dramatically improved by replication of the rigid SU-8 master molds in flexible silicone rubber. Later we discovered that assembly and bonding steps could be accomplished simultaneously by use of substrates pre-coated with very thin ($\approx$2 $\mu$m) films of PDMS. Furthermore, it was shown that these thin films could be prepared in a reliable fashion using off-the-shelf methods. Potential sources of user error during the block assembly process were all but eliminated by incorporating auto-alignment and sealing structures. Lastly, demonstrations of exemplary MAB devices were performed in order to illustrate the variety of potential applications in which MABs can be applied.

## 5.2 Continuing Work

### 5.2.1 Integrated Acoustic Flow Control

The ultimate goal for the acoustic flow control concept presented in Chapter 2 was always to integrate the components on-chip. An embedded microfluidic flow control system possessing the functionality of the prototype macro-system would enable the operation of a complex device using, in theory, only a single on-chip electrical connection — the decoding, amplification, and transduction of the signal would, as in the microsystem, take place on the device itself. Having completed the proof of concept device, future work should focus on miniaturization of the components and potential

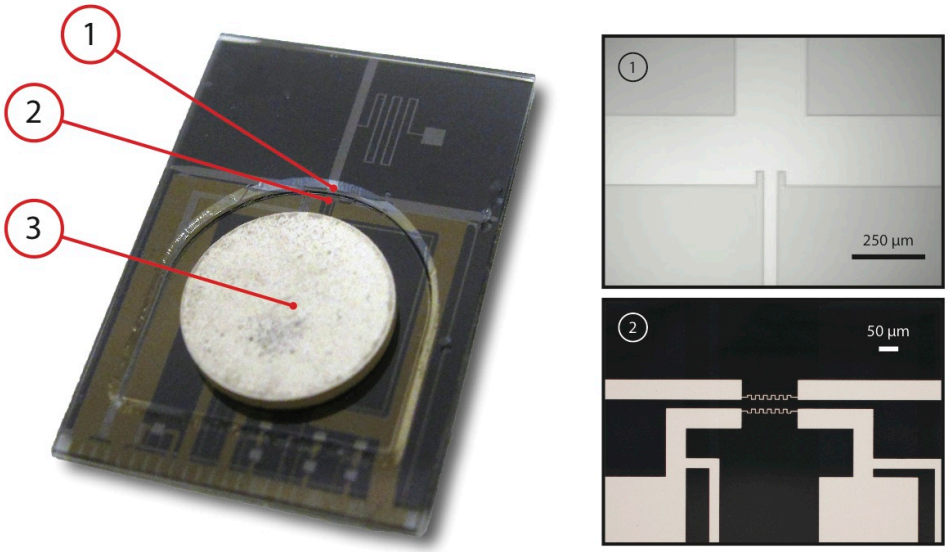


Figure 5.1: Candidate single cavity micro-acoustic design. Device consists of a surface mounted piezoelectric element with integrated diaphragm displacement and flow sensing electronics. (1) Rectifier layout similar to macro-system. (2) Integrated bi-directional hot wire-anemometer for acoustic response characterization. (3) Surface mounted piezoelectric acoustic source. Underneath is a Helmholtz resonance cavity which is separated from the source by a thin glass membrane.

issues that may arise in the process. Miniaturization presents a number of engineering challenges: (1) design and integration of an acoustic source, (2) design of the resonance cavities, (3) design of the rectification structures, and (4) microfabrication and testing.

The effect of viscous damping at the micro-scale will present a significant impedance load for a candidate acoustic source. Such a source must be able to deliver predictable displacements at high frequencies while under load. Microfabricated pumping and propulsion systems, when faced with the same issue, solved the problem by use of high load actuators such as piezoelectric, and electrostatic actuated diaphragms [8, 71]. Piezoelectric drivers are particularly attractive, in this case, as they may be bonded directly to a device without extensive and complex microfabrication. Micro-Helmholtz resonators have been reported in the literature for a number of applications including the generation of synthetic gas jets [71] for micro-thrusters and generation of

aerial entrained flow. Such systems seem to possess sharp resonance and thus are attractive candidates for the implementation of the acoustic flow control concept where it is necessary to make step transitions above and below a rectifier threshold pressure, as we saw in Chapter 2. While other rectifier designs might prove more efficient in generating a flow asymmetry, a layout similar to the macroscopic system should, in theory, function at the micro-scale. The only anticipated operational difference would be an increase in the rectifier threshold pressure due to the reduction in hydraulic diameter. Also, the larger back-pressures presented in the microsystem may require incorporation of converging nozzles at the terminus of the rectifier vents, for example, to introduce an adverse pressure gradient during the compression stroke of the flow cycle. Figure 5.1 shows a candidate single-cavity micro-acoustic design featuring a surface-mounted piezoelectric element with integrated flow and diaphragm displacement sensing. Underneath the piezo element, separated by a thin glass membrane, is a circular Helmholtz cavity with a volume of $\approx 4$ $\mu$L and estimated resonance of 3.89 kHz computed from the lumped element Helmholtz model found in [57]. Experimental characterization of this design will include: calibration of flow and strain sensors, measurement of diaphragm displacement with applied voltage, and mapping of the acoustic response.

### 5.2.2 Multi-Layer MABs

The principle question following the advancements to the MAB concept presented in Chapter 4, is whether or not the MAB approach can be extended to three-dimensions. In addition to planar fluidic networks multi-layer MABs could have an enormous impact on the field as they would allow for integration of active fluidic components such as pumps, valves, and logic structures in addition to planar fluidic networks. Realization of multi-layer MABs depends chiefly upon minimizing variations in block thickness. Deviations on the order of 3-5 $\mu$m, for example, may in fact

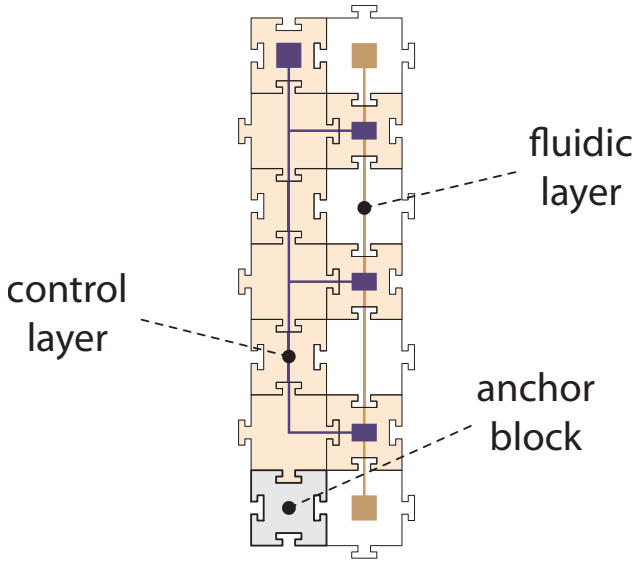


Figure 5.2: Schematic representation of a concept multi-layer MAB device for peristaltic pumping. The device consists of a fluidic layer (bottom), a control layer (top), and a doubly-thick anchor block (gray, lower left) for preserving layer to layer alignment.

prove disastrous for multi-layer construction and should be verified experimentally. Obviously, the most important factor governing the minimum achievable thickness variation is the uniformity of the MAB walls. Unleveled hotplates, as we saw in Appendix A, Figure A.4 can produce deviations $> 100\mu$m. As such, great care must be taken to create perfectly level, clean surfaces for the construction of MAB walls.

An additional option, should narrow tolerances prove to be unreachable with leveling alone, is to replicate the MAB structures in a material such as wax which can be precision milled. Assuming moderately stress-free SU-8 walls, the base silicon substrate should provide an extremely flat reference surface enabling an precision finish end mill to the top surface of the MAB walls to a very high tolerance. Recall also that a slight negative pitch to the MAB walls was observed owing presumably to improper filtering of the exposure source. Elimination of this issue figures heavily in the success of multi-layer MABs and should also be investigated. An example of a

simple multi-layered MAB device, in this case a peristaltic pump, is shown in Figure 5.2. The device features a bottom fluidic layer and a top control layer. Alignment from layer to layer is accomplished using an anchor block which is at least twice as thick as the basic building blocks. Pumping in such a device is accomplished by application of pulsed air pressure to the control layer.

# APPENDICES

# APPENDIX A

# ADVANCES IN MODULAR MICROFLUIDIC CONSTRUCTION

### A.0.3 SU-8 Master Mold: Processing Notes

An unfortunate consequence of spin casting over the top of existing resist structures is that during the spin process, small air bubbles may become entrained in the resist film on the leeward side (*i.e.*, down the gravitational gradient) of the fluidic structures. This is particularly true for the thicker resists and tall rectangular structures employed here. Liberation of trapped air from SU-8 2150 was found, at times, to be quite challenging. The approach which produced the most consistently acceptable resist films consisted of heating the coated wafers on a level hotplate in a solvent rich atmosphere, *i.e.*, fully covered, to 65 °C for $\approx$ 30 minutes. This allows adequate time for free air bubbles to float to the surface and rupture. Bubbles that did not rupture on their own were manually ruptured using the sharp corner of a razor blade or syringe tip. This procedure was repeated as necessary and generally was found to be effective in removing better than 90% of trapped air. The other 10% were typically bubbles either held tightly to the Silicon surface or in the corners

of the existing structures. These remaining few bubbles were removed by carefully dislodging them, again with the corner of a clean razor blade or syringe tip. The resist film, still being highly liquified at this stage, quickly settles into a mirror like surface leaving no trace of a disturbance.

### A.0.4 Mold Replication in Silicone: Processing Notes

A slight roughening of the silicone surface was typically observed following the recovery the negative impression, see Figure A.3. Presumably this is a result of an adverse reaction at the rubber surface during the caustic silanization step. This roughening was found to be benign, however, and did not effect the performance of the resulting MABs. Further investigation is required to definitively identify the source of the roughening. It is possible, for example, that a simple shortening of the silanization treatment time would lessen (if not eliminate) the surface roughness while still providing adequate release characteristics.

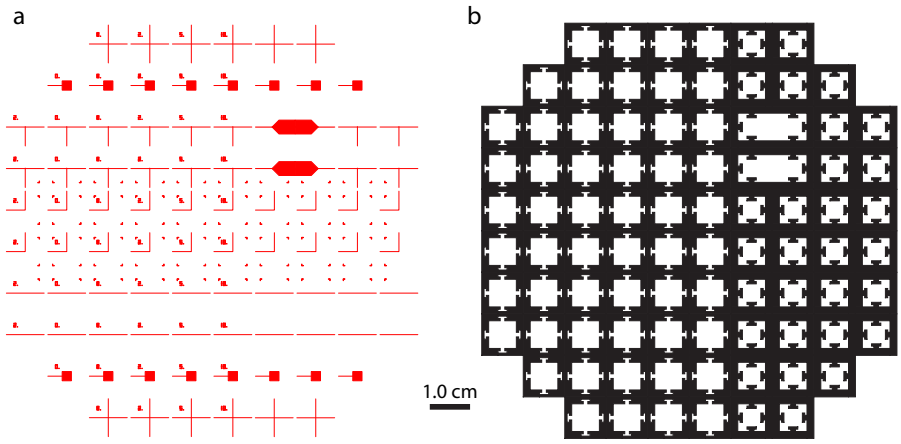


Figure A.1: Current MAB photomask design. (a) Assorted simple fluidic channel layouts consisting of straight, 90° turns, T-junctions, crosses, reaction chambers, and inlets/outlets. Channels are drawn at 200 $\mu$m wide. Numerical indications next to the male pieces correspond to the degree of MAB convexity in $\mu$m. (b) MAB walls for both male and female pieces with principle block dimensions of 8 x 8 mm.

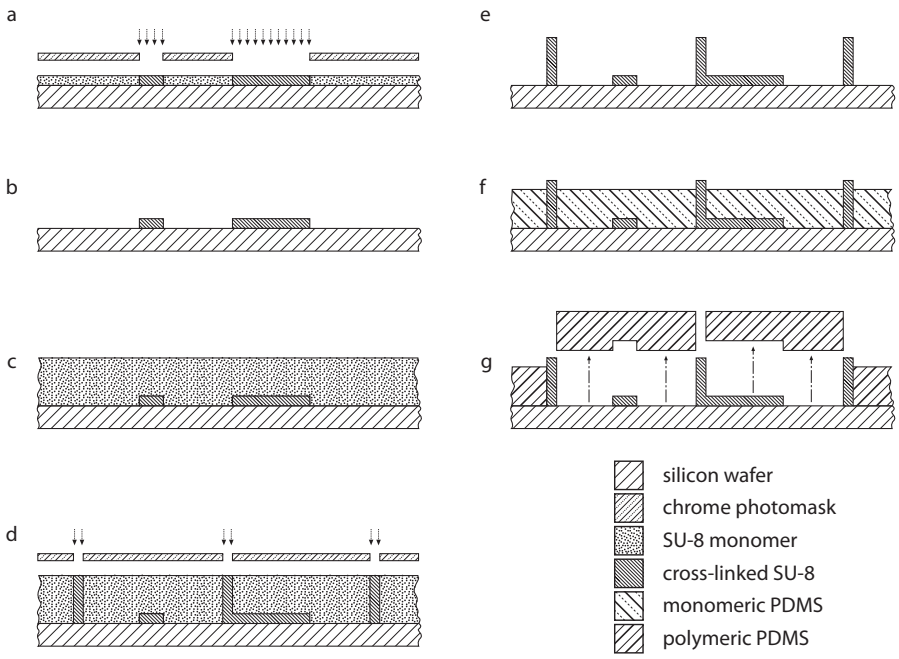


Figure A.2: SU-8 master mold fabrication methodology and original MAB casting technique. (a) SU-8 resist is spun onto a bare silicon wafer according to the patterns for fluidic channels and soft baked on the hot plate for 5 minutes at the 65C and for 20 minutes subsequently at the 95C. The wafer is then exposed on a contact aligner for a length of time appropriate to the resist thickness. (b) After post-exposure baking (PEB) for 3 minutes at the 65C and for 10 minutes at the 95C, the wafer is immersed and developed in fresh SU-8 developer solution. (c) The SU-8 2150 resist is spun to a desired thickness and soft baked for an appropriate length of time ($\approx$ 7 hrs for a 500 $\mu$m film. (d) The wafer then is carefully aligned to a chrome photomask patterned with the MAB walls exposed. (e) After the PEB, the wafer is submersion developed in SU-8 developer. (f) PDMS prepolymer and curing agent (9:1 or 10:1 by weight) is cast against the mold. Then, slightly tilt the mold and scratch the excessive PDMS solution off, using a razor blade. (g) Each cured PDMS block is carefully removed with a sharp aluminum needle.

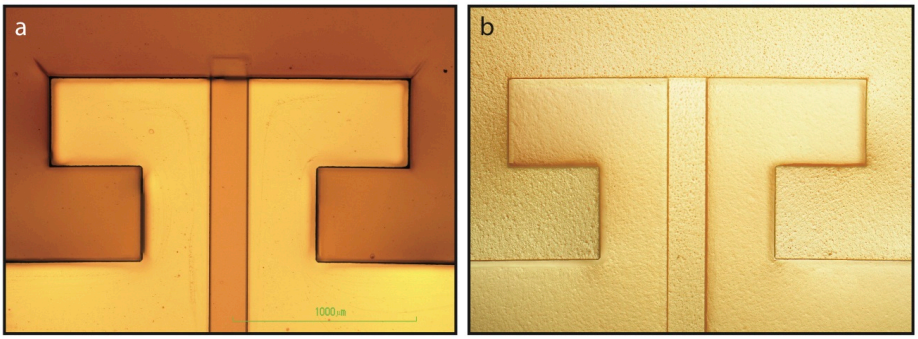


Figure A.3: Observed surface roughening of silicone replicates. (a) Microscope image of original SU-8 master mold following silanization treatment (20 $\mu$L trichlorosilane for 1 hr under closed vacuum). (b) Microscope image of replicate mold in silicone rubber following final silanization treatment exhibiting a slightly roughened surface topology.

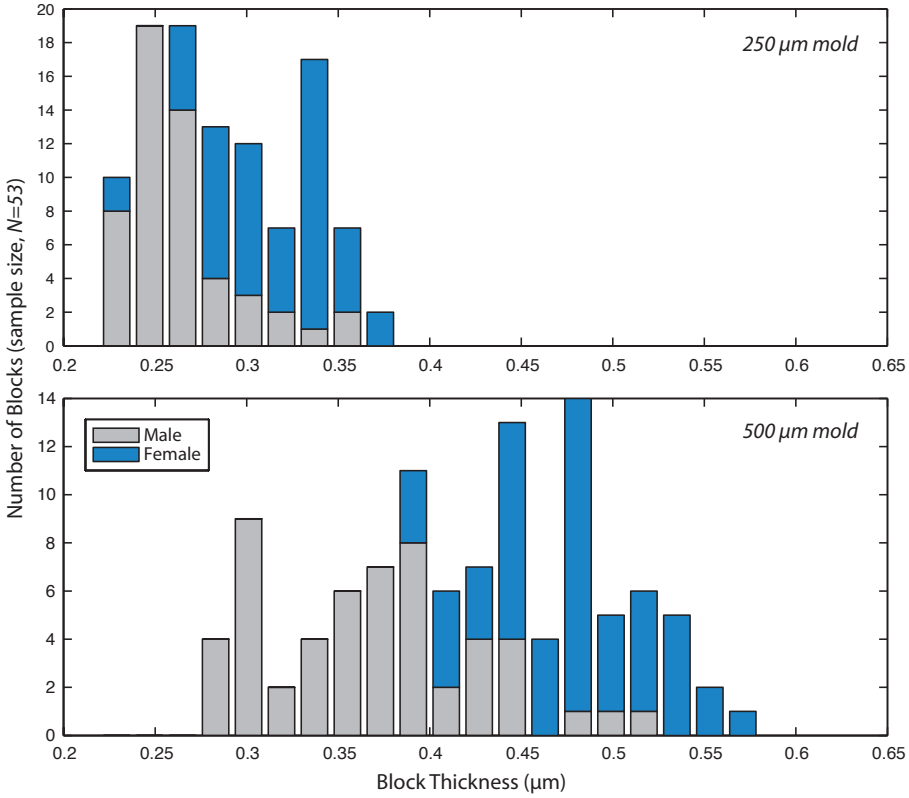


Figure A.4: Variations in MAB thickness. (top) Thickness distribution of male and female MABs taken from a 250 $\mu$m mold. (bottom) Thickness distribution of male and female MABs taken from a 500 $\mu$m mold.

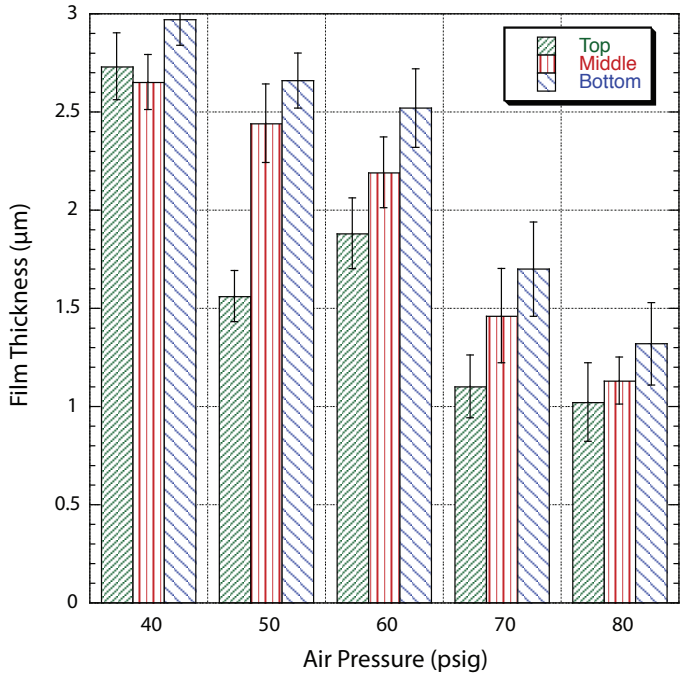


Figure A.5: Systematic variation in film thickness of prepared substrates. (main plot) Variation in thin-film thickness as a function of location on the substrate (top, middle, bottom). Note: *top* refers to the beginning of the air-jet path (*inset*, Figure 4.6b).

# BIBLIOGRAPHY

# BIBLIOGRAPHY


[1] P.K. Wong, T.H. Wang, J.H. Deval, and C.M. Ho. Electrokinetics in micro devices for biotechnology applications. *Mechatronics, IEEE/ASME Transactions on*, 9(2):366–376, 2004.

[2] W.E. Morf, O.T. Guenat, and N.F. De Rooij. Partial electroosmotic pumping in complex capillary systems:: Part 1: Principles and general theoretical approach. *Sensors and Actuators B: Chemical*, 72(3):266–272, 2001.

[3] J.R. Melcher and M.S. Firebaugh. Traveling-wave bulk electroconvection induced across a temperature gradient. *Physics of Fluids*, 10:1178, 1967.

[4] M. Vallet, M. Vallade, and B. Berge. Limiting phenomena for the spreading of water on polymer films by electrowetting. *The European Physical Journal B-Condensed Matter and Complex Systems*, 11(4):583–591, 1999.

[5] D. Juncker, H. Schmid, U. Drechsler, H. Wolf, M. Wolf, B. Michel, N. de Rooij, and E. Delamarche. Autonomous microfluidic capillary system. *Anal. Chem*, 74(24):6139–6144, 2002.

[6] P.D.I. Fletcher, S.J. Haswell, E. Pombo-Villar, B.H. Warrington, P. Watts, S.Y.F. Wong, and X. Zhang. Micro reactors: principles and applications in organic synthesis. *Tetrahedron*, 58(24):4735–4757, 2002.

[7] D.J. Laser and J.G. Santiago. A review of micropumps. *Journal of micromechanics and microengineering*, 14:R35, 2004.

[8] J.C. Rife, M.I. Bell, J.S. Horwitz, M.N. Kabler, R.C.Y. Auyeung, and W.J. Kim. Miniature valveless ultrasonic pumps and mixers. *Sensors & Actuators: A. Physical*, 86(1-2):135–140, 2000.

[9] R. Gorkin, J. Park, J. Siegrist, M. Amasia, B.S. Lee, J.M. Park, J. Kim, H. Kim, M. Madou, and Y.K. Cho. Centrifugal microfluidics for biomedical applications. *Lab on a Chip*, 10(14):1758–1773, 2010.

[10] K. Sritharan, C.J. Strobl, M.F. Schneider, A. Wixforth, and Z. Guttenberg. Acoustic mixing at low Reynolds numbers. *Applied Physics Letters*, 88:054102, 2006.

[11] D.C. Duffy, J.C. McDonald, O.J.A. Schueller, and G.M. Whitesides. Rapid prototyping of microfluidic systems in poly (dimethylsiloxane). *Anal. Chem*, 70(23):4974–4984, 1998.

[12] A. Tan, K. Rodgers, J.P. Murrihy, C. O'Mathuna, and J.D. Glennon. Rapid fabrication of microfluidic devices in poly (dimethylsiloxane) by photocopying. *Lab on a Chip*, 1(1):7–9, 2001.

[13] A. Grimes, D.N. Breslauer, M. Long, J. Pegan, L.P. Lee, and M. Khine. Shrinky-dink microfluidics: rapid generation of deep and rounded patterns. *Lab on a Chip*, 8(1):170–172, 2008.

[14] J.C. McDonald and G.M. Whitesides. Poly (dimethylsiloxane) as a material for fabricating microfluidic devices. *Acc. Chem. Res*, 35(7):491–499, 2002.

[15] M. Rhee and M.A. Burns. Microfluidic assembly blocks. *Lab on a Chip*, 8(8):1365–1373, 2008.

[16] K.A. Shaikh, K.S. Ryu, E.D. Goluch, J.M. Nam, J. Liu, C.S. Thaxton, T.N. Chiesl, A.E. Barron, Y. Lu, C.A. Mirkin, et al. A modular microfluidic architecture for integrated biochemical analysis. *Proceedings of the National Academy of Sciences of the United States of America*, 102(28):9745, 2005.

[17] P.K. Yuen. SmartBuild–A truly plug-n-play modular microfluidic system. *Lab on a Chip*, 8(8):1374–1378, 2008.

[18] P. Grodzinski, J. Yang, R.H. Liu, and M.D. Ward. A modular microfluidic system for cell pre-concentration and genetic sample preparation. *Biomedical Microdevices*, 5(4):303–310, 2003.

[19] G.M. Greenway, S.J. Haswell, D.O. Morgan, V. Skelton, and P. Styring. The use of a novel microreactor for high throughput continuous flow organic synthesis. *Sensors & Actuators: B. Chemical*, 63(3):153–158, 2000.

[20] E.M. Chan, A.P. Alivisatos, and R.A. Mathies. High-temperature microfluidic synthesis of CdSe nanocrystals in nanoliter droplets. *JACS*, 12:17, 2005.

[21] D.C. Pregibon, M. Toner, and P.S. Doyle. Multifunctional encoded particles for high-throughput biomolecule analysis. *Science*, 315(5817):1393, 2007.

[22] B. Zheng, J.D. Tice, and R.F. Ismagilov. Formation of droplets of alternating composition in microfluidic channels and applications to indexing of concentrations in droplet-based assays. *Analytical Chemistry*, 76(17):4977, 2004.

[23] S.Y. Teh, R. Lin, L.H. Hung, and A.P. Lee. Droplet microfluidics. *Lab on a Chip*, 8(2):198–220, 2008.

[24] M.A. Eddings and B.K. Gale. A pdms-based gas permeation pump for on-chip fluid handling in microfluidic devices. *Journal of Micromechanics and Microengineering*, 16(11):2396–2402, 2006.

[25] R. Pal, M. Yang, R. Lin, B.N. Johnson, N. Srivastava, S.Z. Razzacki, K.J. Chomistek, D.C. Heldsinger, R.M. Haque, and V.M. et al. Ugaz. An integrated microfluidic device for influenza and other genetic analyses. *Lab on a Chip*, 5(10):1024–1032, 2005.

[26] D.S. Chang, S.M. Langelier, and M.A. Burns. An electronic venturi-based pressure microregulator. *Lab on a Chip*, 7(12):1791–1799, 2007.

[27] M.A. Unger, H.P. Chou, T. Thorsen, A. Scherer, and S.R. Quake. Monolithic microfabricated valves and pumps by multilayer soft lithography. *Science*, 288(5463):113, 2000.

[28] T. Thorsen, S.J. Maerkl, and S.R. Quake. Microfluidic large-scale integration. *Science*, 298(5593):580, 2002.

[29] Z. Guttenberg, H. Müller, H. Habermüller, A. Geisbauer, J. Pipper, J. Felbel, M. Kielpinski, J. Scriba, and A. Wixforth. Planar chip device for pcr and hybridization with surface acoustic wave pump. *Lab on a Chip*, 5(3):308–317, 2005.

[30] R.J. Dijkink, J.P. van der Dennen, C.D. Ohl, and A. Prosperetti. The acoustic scallop: a bubble-powered actuator. *J. Micromech. Microeng*, 16:1653–9, 2006.

[31] F. Petersson, L. Aberg, A.M. Sward-Nilsson, and T. Laurell. Free flow acoustophoresis: Microfluidic-based mode of particle and cell separation. *Analytical Chemistry*, 79(14):5117–5123, 2007.

[32] L. Puskar, R. Tuckermann, T. Frosch, J. Popp, V. Ly, D. McNaughton, and B.R. Wood. Raman acoustic levitation spectroscopy of red blood cells and plasmodium falciparum trophozoites. *Lab on a Chip*, 7(9):1125–1131, 2007.

[33] J. Lighthill. Acoustic streaming. *(Institute of Acoustics, Spring Meeting, Cambridge, England, Apr. 6, 1978.) Journal of Sound and Vibration*, 61, 1978.

[34] S.W. Schneider, S. Nuschele, A. Wixforth, C. Gorzelanny, A. Alexander-Katz, R.R. Netz, and M.F. Schneider. Shear-induced unfolding triggers adhesion of von Willebrand factor fibers. *Proceedings of the National Academy of Sciences*, 104(19):7899, 2007.

[35] A. Groisman and S.R. Quake. A microfluidic rectifier: anisotropic flow resistance at low reynolds numbers. *Physical Review Letters*, 92(9):94501, 2004.

[36] V. Tesař. Configurations of fluidic actuators for generating hybrid-synthetic jets. *Sensors & Actuators: A. Physical*, 138(2):394–403, 2007.

[37] J.V. Sánchez-Pérez, D. Caballero, R. Martinez-Sala, C. Rubio, J. Sánchez-Dehesa, F. Meseguer, J. Llinares, and F. Gálvez. Sound attenuation by a two-dimensional array of rigid cylinders. *Physical Review Letters*, 80(24):5325–5328, 1998.

[38] J. Wen, G. Wang, D. Yu, H. Zhao, and Y. Liu. Theoretical and experimental investigation of flexural wave propagation in straight beams with periodic structures: Application to a vibration isolation structure. *Journal of Applied Physics*, 97:114907, 2005.

[39] J.O. Vasseur, P.A. Deymier, A. Khelif, P. Lambin, B. Djafari-Rouhani, A. Akjouj, L. Dobrzynski, N. Fettouhi, and J. Zemmouri. Phononic crystal with low filling fraction and absolute acoustic band gap in the audible frequency range: A theoretical and experimental study. *Physical Review E*, 65(5):56608, 2002.

[40] M.H. Lu, C. Zhang, L. Feng, J. Zhao, Y.F. Chen, Y.W. Mao, J. Zi, Y.Y. Zhu, S.N. Zhu, and N.B. Ming. Negative birefraction of acoustic waves in a sonic crystal. *Nature Materials*, 6(10):744–748, 2007.

[41] M. Ambati, N. Fang, C. Sun, and X. Zhang. Surface resonant states and superlensing in acoustic metamaterials. *Physical Review B*, 75(19):195447, 2007.

[42] M.F. Su, R.H. Olsson III, Z.C. Leseman, and I. El-Kady. Realization of a phononic crystal operating at gigahertz frequencies. *Applied Physics Letters*, 96:053111, 2010.

[43] M. Torres, F.R. Montero de Espinosa, and J.L. Aragon. Ultrasonic wedges for elastic wave bending and splitting without requiring a full band gap. *Physical review letters*, 86(19):4282–4285, 2001.

[44] A. Khelif, A. Choujaa, S. Benchabane, B. Djafari-Rouhani, and V. Laude. Guiding and bending of acoustic waves in highly confined phononic crystal waveguides. *Applied Physics Letters*, 84:4400, 2004.

[45] P.D.C. King and T.J. Cox. Acoustic band gaps in periodically and quasiperiodically modulated waveguides. *Journal of Applied Physics*, 102:014902, 2007.

[46] Y. Pennec, B. Djafari-Rouhani, J.O. Vasseur, A. Khelif, and P.A. Deymier. Tunable filtering and demultiplexing in phononic crystals with hollow cylinders. *Physical Review E*, 69(4):46608, 2004.

[47] C.J. Rupp, M.L. Dunn, and K. Maute. Switchable phononic wave filtering, guiding, harvesting, and actuating in polarization-patterned piezoelectric solids. *Applied Physics Letters*, 96:111902, 2010.

[48] R.H.O.I. El-Kady. Microfabricated phononic crystal devices and applications. *Measurement Science and Technology*, 20(1):2002, 2009.

[49] Z. Liu, X. Zhang, Y. Mao, Y.Y. Zhu, Z. Yang, C.T. Chan, and P. Sheng. Locally resonant sonic materials. *Science*, 289(5485):1734, 2000.

[50] W.M. Robertson and J.F. Rudy III. Measurement of acoustic stop bands in two-dimensional periodic scattering arrays. *The Journal of the Acoustical Society of America*, 104:694, 1998.

[51] T. Gorishnyy, C.K. Ullal, M. Maldovan, G. Fytas, and E.L. Thomas. Hypersonic phononic crystals. *Physical review letters*, 94(11):115501, 2005.

[52] R.H. Olsson III, I.F. El-Kady, M.F. Su, M.R. Tuck, and J.G. Fleming. Microfabricated VHF acoustic crystals and waveguides. *Sensors and Actuators A: Physical*, 145:87–93, 2008.

[53] N.K. Kuo, C. Zuo, and G. Piazza. Microscale inverse acoustic band gap structure in aluminum nitride. *Applied Physics Letters*, 95:093501, 2009.

[54] R. Wei, B. Wu, C. He, and H. Zhao. Phononic band structure in a two-dimensional hybrid triangular graphite lattice. *Physica B: Condensed Matter*, 2009.

[55] E.N. Economou and M.M. Sigalas. Classical wave propagation in periodic structures: Cermet versus network topology. *Physical Review B*, 48(18):13434–13438, 1993.

[56] Y.Z. Wang, F.M. Li, W.H. Huang, and Y.S. Wang. Effects of inclusion shapes on the band gaps in two-dimensional piezoelectric phononic crystals. *Journal of Physics: Condensed Matter*, 19:496204, 2007.

[57] L.E. Kinsler, A.R. Frey, A.B. Coppens, and J.V. Sanders. *Fundamentals of acoustics*. Wiley, 1999.

[58] J. El-Ali, P.K. Sorger, and K.F. Jensen. Cells on chips. *Nature*, 442(7101):403–411, 2006.

[59] M.A. Burns. Everyone's a (future) chemist. *Science*, 296(5574):1818–1819, 2002.

[60] D.R. Meldrum and M.R. Holl. Microfluidics: Microscale bioanalytical systems. *Science*, 297(5584):1197, 2002.

[61] M.A. Burns, B.N. Johnson, S.N. Brahmasandra, K. Handique, J.R. Webster, M. Krishnan, T.S. Sammarco, P.M. Man, D. Jones, and D. et al. Heldsinger. An integrated nanoliter dna analysis device. *Science*, 282(5388):484, 1998.

[62] J.J. Agresti, E. Antipov, A.R. Abate, K. Ahn, A.C. Rowat, J.C. Baret, M. Marquez, A.M. Klibanov, A.D. Griffiths, and D.A. Weitz. Ultrahigh-throughput screening in drop-based microfluidics for directed evolution. *Proceedings of the National Academy of Sciences*, 107(9):4004, 2010.

[63] P.J. Hung, P.J. Lee, P. Sabounchi, R. Lin, and L.P. Lee. Continuous perfusion microfluidic cell culture array for high-throughput cell-based assays. *Biotechnology and bioengineering*, 89(1):1–8, 2005.

[64] M.A. McClain, C.T. Culbertson, S.C. Jacobson, N.L. Allbritton, C.E. Sims, and J.M. Ramsey. Microfluidic devices for the high-throughput chemical analysis of cells. *Anal. Chem*, 75(21):5646–5655, 2003.

[65] D. Huh, B.D. Matthews, A. Mammoto, M. Montoya-Zavala, H.Y. Hsin, and D.E. Ingber. Reconstituting organ-level lung functions on a chip. *Science*, 328(5986):1662, 2010.

[66] G.M. Whitesides. The origins and the future of microfluidics. *Nature*, 442(7101):368–373, 2006.

[67] A. Liu, F. He, K. Wang, T. Zhou, Y. Lu, and X. Xia. Rapid method for design and fabrication of passive micromixers in microfluidic devices using a direct-printing process. *Lab on a Chip*, 5(9):974–978, 2005.

[68] B. Li, M. Liu, and Q. Chen. Low-stress ultra-thick SU-8 UV photolithography process for MEMS. *Journal of Microlithography, Microfabrication, and Microsystems*, 4:043008, 2005.

[69] M. Rhee and M.A. Burns. Microfluidic pneumatic logic circuits and digital pneumatic microprocessors for integrated microfluidic systems. *Lab on a Chip*, 9(21):3131, 2009.

[70] B. Mosadegh, C.H. Kuo, Y.C. Tung, Y. Torisawa, T. Bersano-Begey, H. Tavana, and S. Takayama. Integrated elastomeric components for autonomous regulation of sequential and oscillatory flow switching in microfluidic devices. *Nature Physics*, 6(6):433–437, 2010.

[71] T.K.A. Chou, K. Najafi, M.O. Muller, L.P. Bernal, and P.D. Washabaugh. Characterization of micromachined acoustic ejector and its applications. In *Micro Electro Mechanical Systems, 2002. The Fifteenth IEEE International Conference on*, pages 264–267. IEEE, 2002.